Electronic Supplementary Information (ESI)

Hierarchical superparamagnetic Metal-Organic Frameworks nanovectors as anti-inflammatory nanomedicine.†

Heng Zhao,[a] Saad Sene,[b] Angelika M. Mielcarek,[a] Sylvain Miraux,[c] Nicolas Menguy,[d] Dris Ihiawakrim,[e] Ovidiu Ersen,[e] Christine Péchoux,[f] Nathalie Guillou,[b] Joseph Scola,[g] Jean-Marc Grenèche,[h] Farid Nouar,[a] Simona Mura,[i¶] Florent Carn,[j] Florence Gazeau,[j] Eddy Dumas,[b] Christian Serre,*[,a] and Nathalie Steunou*[,a,b]

[a]Institut des Matériaux Poreux de Paris, ENS, ESPCI Paris, CNRS, PSL university, Paris, France. E-mail: christian.serre@ens.fr, nathalie.steunou@uvsq.fr.

[b]Institut Lavoisier de Versailles, UMR CNRS 8180, Université de Versailles St Quentin en Yvelines, Université Paris Saclay, Versailles, France.

[c]Centre de Résonance Magnétique des Systèmes Biologiques, UMR5536, CNRS/Univ. Bordeaux 33076 Bordeaux, France.

[d]Sorbonne Université, UMR CNRS 7590, MNHN, IRD, Institut de Minéralogie, de Physique des Matériaux et de Cosmochimie, IMPMC, 75005 Paris, France.

[e]Institut de Physique et Chimie des Matériaux de Strasbourg (IPCMS) UMR 7504 CNRS – Université de Strasbourg, 23 rue du Loess 67034 Strasbourg Cedex 2, France.

[f]Université Paris-Saclay, INRAE, AgroParisTech, GABI, 78350, Jouy-en-Josas, France.

[g]Groupe d'Etudes de la Matière Condensée, UMR CNRS 8635, Université de Versailles St Quentin en Yvelines, Université Paris Saclay 78035 Versailles, France.

[h]Institut des Molécules et des Matériaux du Mans, UMR CNRS 6283, Université du Maine, 72085 Le Mans, France.

[i]Institut Galien Paris-Saclay, UMR 8612, CNRS, Université Paris-Saclay, Faculté de Pharmacie, 5 rue Jean-Baptiste Clément, F92296 Châtenay-Malabry cedex, France.

[j]Laboratoire Matière et Systèmes Complexes (MSC), UMR CNRS 7057, Université de Paris, 75013 Paris, France.

Table of Contents

1- Chemicals

All chemicals were used as received without any further purification: Iron(III) chloride hexahydrate ($FeCl_3 \cdot 6H_2O$; 98%), iron(II) chloride tetrahydrate ($FeCl_2 \cdot 4H_2O$; 98%), iron(III) nitrate nonahydrate ($Fe(NO_3)_3 \cdot 9H_2O$; 98%) and L-Glutathione reduced (GSH, >98%) were purchased from Alfa Aesar. 1,3,5-benzenetricarboxylic acid (1,3,5-BTC; 95%), Lipopolysaccharides (LPS), 2′,7′-Dichlorofluorescin Diacetate (DCF-DA), glutaraldehyde solution 25% and sodium cacodylate trihydrate (≥ 98%) were purchased from Sigma Aldrich. Methotrexate (MTX, >98%) was purchased from TCI. Doxorubicin HCl was purchased from Carbosynth (UK). Cell counting kit-8 (CCK-8), Calcein-AM solution were purchased from Dojindo. Propidium Iodide (PI) was purchased from Invitrogen. Hoechst33342 were purchased from Abcam. Proinflammatory cytokines (IL-1β, IL-6 and TNF-α) Duoset Elisa Kits were purchased from R&D Systems. Physiological media were prepared with phosphate buffered saline (PBS, Sigma Aldrich) and bovine serum albumin (BSA, Sigma Aldrich). Ultrapure water was obtained with the Milli Q purification system (Merck Millipore, France).

2-Characterization techniques

Powder X-ray diffraction patterns (PXRD) were collected with a Siemens D5000 diffractometer (θ-2θ) using Cu Kα radiation (λ = 1.5418 Å). For USPIO@MIL NPs Refinements were carried out with the TOPAS program. Profile fittings and Rietveld refinement in the case of the maghemite for USPIO(10)@MIL sample were performed using fundamental parameters approach to model the instrument function and determine crystallite size. Thermogravimetric analyses (TGA) were performed on a Perkins Elmer SDA 6000 apparatus. Samples were heated up to 600 °C with a heating rate of 5 °C·min^{-1} under an oxygen atmosphere. Transmission IR spectra were recorded in the 400-4000 cm^{-1} range, with 4 cm^{-1} resolution on a Nicolet Nexus spectrometer. N_2 sorption isotherms were obtained at 77 K

using a Belsorp Mini (Bel, Japan). Prior to the analysis, approximately 30 mg of samples were evacuated for 5 h at 120 °C under primary vacuum. Brunauer-Emmett-Teller (BET) surface and pore volume were estimated at a relative pressure lower than 0.25. TEM observations were performed using a Zeiss EM902 Transmission Electron Microscope (Plateforme de microscopie et d'imagerie de l'INRA, Jouy en Josas, France). TEM images were also recorded on a JEOL 2100F microscope operating at 200 kV, equipped with a Schottky emission gun, a high resolution UHR pole piece and a Gatan US4000 CCD camera. High-angle annular dark field imaging in scanning transmission electron microscope mode (STEM-HAADF) experiments were performed on a JEOL JEM 2100F microscope installed at IMPMC (Paris, France), operating at 200 kV, equipped with a field emission gun, a JEOL detector with an ultrathin window allowing detection of light elements and a scanning TEM (STEM) device, which allows Z-contrast imaging in HAADF mode. Samples were prepared by deposition of one droplet of colloidal suspensions onto a carbon-coated copper grid and left to dry in air. Electron tomography analysis was carried out in the cryo-mode using a JEOL 2100 FEG S/TEM microscope operated at 200 kV equipped with a spherical aberration corrector. For the acquisition of high-angular annular dark field (HAADF) images in the scanning TEM (STEM) mode, we used a spot size of 0.13 nm, a current density of 140 pA, a camera focal length of 8 cm, corresponding to inner and outer diameters of the annular detector of about 73 and 194 mrad. The acquisition of tilt series was performed using the tomography plug-in of the Digital Micrograph software, which controls the specimen tilt step by step, the defocusing and the specimen drift. The HAADF and BF tilt series in the STEM were acquired simultaneously by using the ADF and BF detectors and tilting the specimen in the angular range of ± 60° using an increment of 2° in the equal mode, giving thus a total of 61 images in each series. The as-obtained images were spatially aligned by cross correlating consecutive images using IMOD software. For the volume calculation, we used the algebraic reconstruction technique (ART)

implemented in the TomoJ plugin working in the ImageJ software. Finally, the visualization and the analysis of the volumes were carried out using the displaying capabilities and the isosurface rendering method in the Slicer software. The particle diameter of γ-Fe_2O_3, MIL-100(Fe) and USPIO(20)@MIL was measured by Dynamic Light Scattering (DLS) on a Zetasizer NanoZS (Malvern Instruments). NPs (~ 0.1 - 0.2 $mg \cdot mL^{-1}$) were dispersed at RT in aqueous solutions by using an ultrasound tip (Digital Sonifer 450, Branson) during 1 minute at 10% amplitude. Their surface charge was also evaluated by recording ζ-potential with the Zetasizer NanoZS.

3-Synthesis and characterization of MIL-100(Fe) nanoparticles

Synthesis of MIL-100(Fe) nanoparticles

0.72 g of $Fe(NO_3)_3 \cdot 9H_2O$ (1.78 mmol) was dissolved in 90 mL of distilled water. 0.25 g of trimesic acid (1.19 mmol) was then added to this solution and the suspension was allowed to stir for 48 h at room temperature. The mixture was then centrifuged at 14500 rpm for 10 min. An orange solid was thus obtained. The as-synthesized MIL-100(Fe) NPs were then washed by two centrifugation/redispersion cycles in water followed by two centrifugation/redispersion cycles in absolute ethanol. The MIL-100(Fe) NPs were stored in EtOH and could be redispersed in water before use.

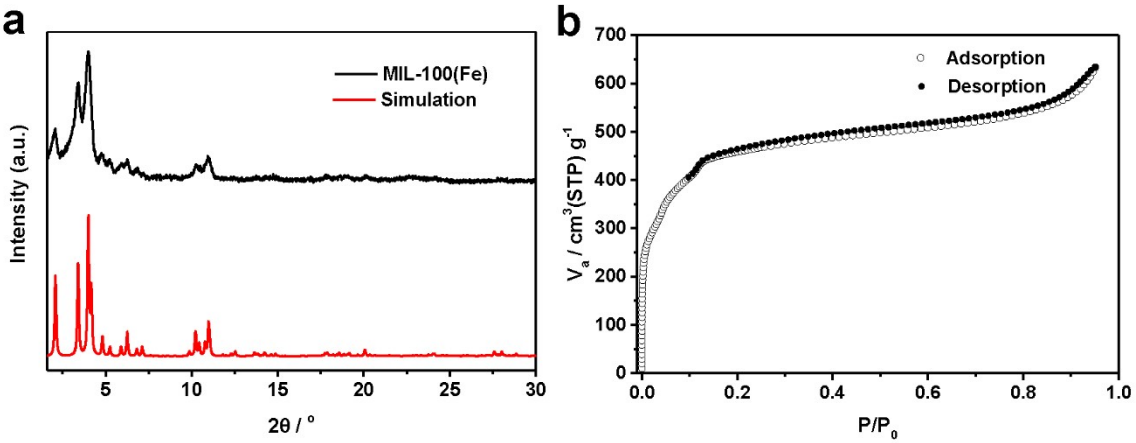

Figure S1. Characterizations of MIL-100(Fe): a) Powder X-Ray diffraction pattern measurements and (b) Nitrogen adsorption and desorption isotherms.

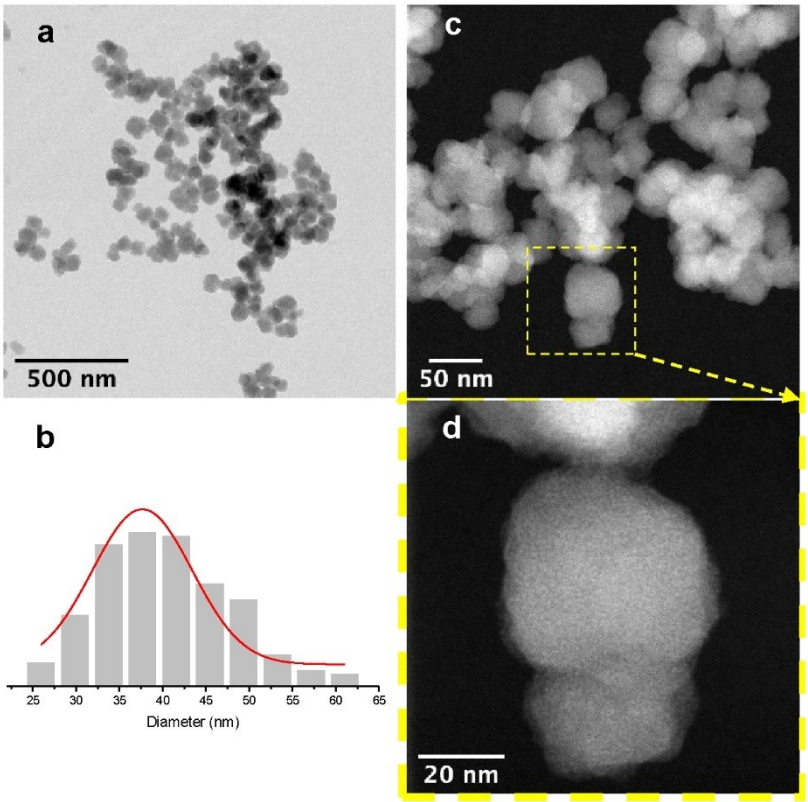

Figure S2. a) TEM bright field and (c-d) STEM-HAADF images of MIL-100(Fe) nanoparticles, (b) Size distribution of MIL-100(Fe) nanoparticles. (Diameter = 40 ± 8 nm)

The Bragg peaks of the powder X-ray diffraction (PXRD) patterns are consistent with the crystalline structure of MIL-100(Fe) NPs. N_2 adsorption/desorption isotherm is typical of MIL-

100(Fe) with a BET surface area of 1700 $m^2 \cdot g^{-1}$. TEM showed spheroidal MIL-100(Fe) NPs with a diameter of 40 nm.

4-Synthesis and characterization of maghemite (γ-Fe_2O_3) nanoparticles (USPIO)

20 mL of sodium hydroxide (15 $mol \cdot L^{-1}$) were mixed under vigorous stirring with an aqueous solution containing 20 mL of $FeCl_3 \cdot 6H_2O$ (1 $mol \cdot L^{-1}$) and 5 mL of $FeCl_2 \cdot 4H_2O$ (2 $mol \cdot L^{-1}$) in HCl (2 $mol \cdot L^{-1}$). A black precipitate was obtained by magnetic settling and washed with 20 mL of water. The precipitate was then stirred for 15 min in 30 mL of HNO_3 (2 $mol \cdot L^{-1}$). For a complete oxidation of magnetite to maghemite, the precipitate was then mixed with 10 mL of $Fe(NO_3)_3 \cdot 9H_2O$ (0.35 $mol \cdot L^{-1}$) at 80 °C for 30 min. The precipitate was finally peptised in 30 mL of HNO_3 (2 $mol \cdot L^{-1}$) for 10 minutes before being washed 3 times with 10 mL of acetone. The colloidal solution of γ-Fe_2O_3 was stored in 20 mL of water with a final pH between 2 and 3 and a weight concentration around 65 $g \cdot L^{-1}$.

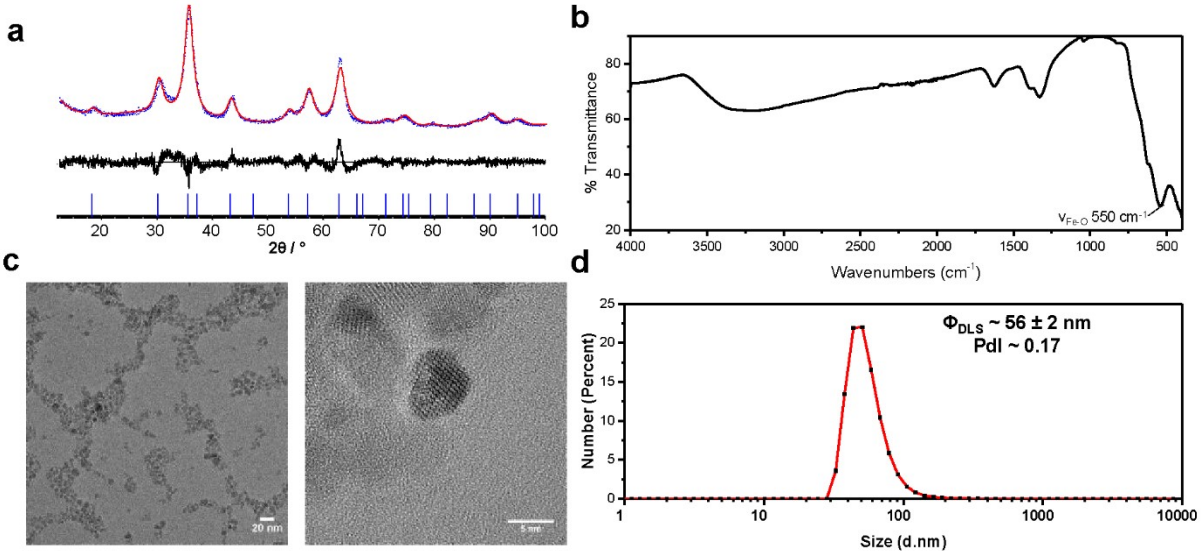

Figure S3. Characterizations of maghemites γ-Fe_2O_3: a) Rietveld-refinement on γ-Fe_2O_3 diffractogram; b) Infrared spectrum; c) HRTEM images; d) Size distribution by DLS.

X-Ray diffraction measurements showed that the nanoparticles present the typical spinel structure. The calculated lattice parameter, 0.8360 (3) nm, is close to that of maghemite (0.8346 nm, JCPDS file 39-1346). The mean size of the nanoparticles estimated from X-ray pattern (5.4 ± 0.1 nm) is also in agreement with the TEM observations (7 ± 3 nm). The IR band of γ-Fe_2O_3 at 550 cm^{-1} was assigned to stretching vibration of the Fe-O bond.

5-Synthesis and characterization of USPIO(20)@MIL nano-objects

Synthesis of USPIO@MIL nano-objects

The USPIO@MIL nano-objects were prepared by adding under stirring a colloidal solution containing 70 or 30 mg of maghemite NPs to an aqueous solution of $Fe(NO_3)_3 \cdot 9H_2O$ (70 mL, 0.72 g). The suspension was then sonicated for 2 minutes at 20% amplitude. 250 mg of trimesic acid (1.2 mmol) were then added and the mixture was stirred for 24 h at RT. The brown precipitate was isolated by magnetic settling and then centrifuged at 14500 rpm for 10 min. The solid was then washed by one centrifugation/redispersion cycle in water followed by three centrifugation/redispersion cycles in absolute ethanol. The USPIO@MIL NPs were stored in EtOH and could be redispersed in water before use. By using 70 or 30 mg of γ-Fe_2O_3 NP during the synthesis, it was possible to obtain USPIO@MIL nano-objects with 20 or 10 wt% of γ-Fe_2O_3 content, respectively.

Determination of the USPIO content

After drying in vacuum overnight, ~5 mg USPIO(20)@MIL and MIL-100(Fe) were accurately weighed and then degraded with 1 mL concentrated HCl under 80 °C for 12 h. After centrifugation (13400 rpm, 15min), Fe ion in the supernatant was separated from BTC (white precipitate) because BTC cannot be dissolved in concentrated HCl. The supernatant was diluted by 2% HNO_3 solution for ICP MS analysis (Fe ion) and the precipitate was then dissolved in 1 mL EtOH for HPLC test. The mobile phase of HPLC is 50:50 v/v methanol : phosphate buffer (0.02 M NaH_2PO_4 and Na_2HPO_4, pH 2.5, adjusted by H_3PO_4). A flow rate of 0.8 mL/min and a sample injection volume of 50 µL were used during all analyses.

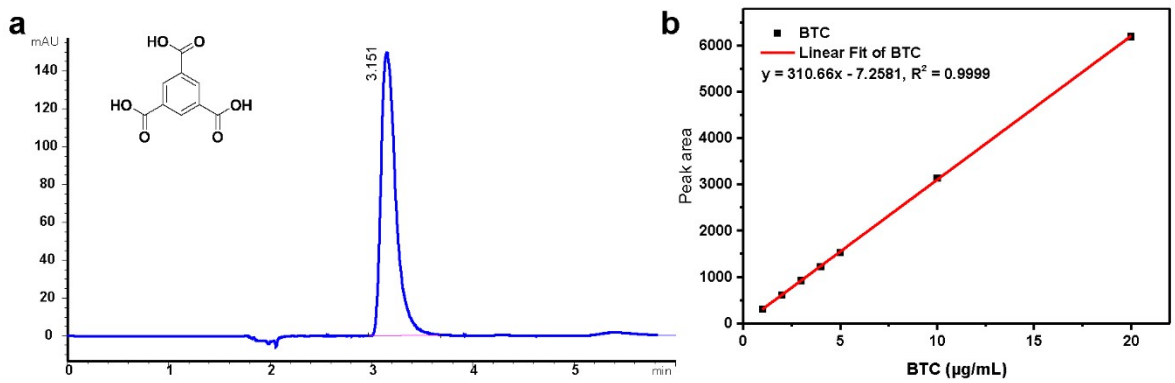

Figure S4. The high-performance liquid chromatography (HPLC) spectrum and calibration curve of BTC.

Table S1. The ratio of Fe ion (ICP-MS) to BTC (HPLC) of MIL-100(Fe) and USPIO(20)@MIL.

Sample	Weight (mg)	ICP-Fe (mg)	HPLC-BTC (mg)	Fe : BTC (mol/mol)	Fe_2O_3 wt%
USPIO(20)@MIL	5.2	1.42	1.85	2.896	20.5
MIL-100(Fe)	4.7	0.667	1.67	1.502	

In bare MIL-100(Fe), the ratio of Fe to BTC was close to 1.5, which was in consistent with the theoretical one. According to the calculation below, the weight ratio of γ-Fe_2O_3 in USPIO(20)@MIL was ~20%.

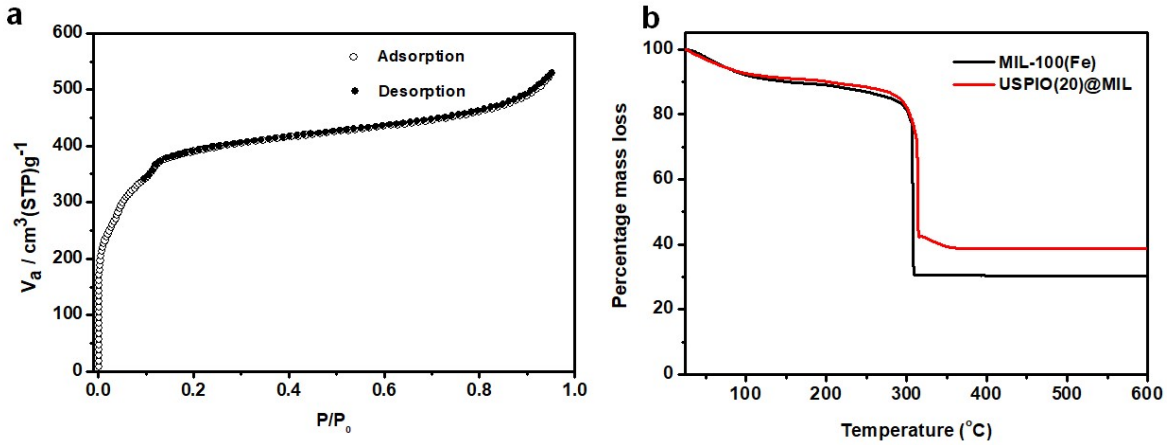

Figure S5. a) Nitrogen sorption isotherms at 77 K (P_0 = 1atm) and (b) TGA of USPIO(20)@MIL.

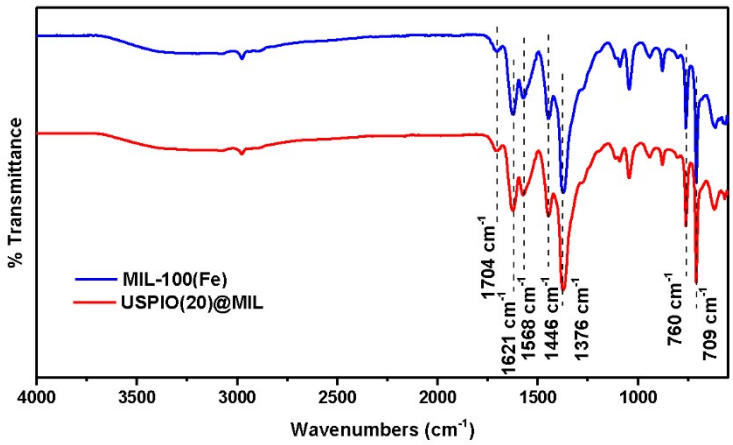

Figure S6. FT-IR spectra of MIL-100(Fe) and USPIO(20)@MIL.

The FT-IR spectra of both MIL-100(Fe) and and USPIO(20)@MIL exhibit characteristic vibration bands at 1621, 1568, 1446, 1376, 760 and 709 cm^{-1}. The bands at 1624 and 1376 cm^{-1} are assigned to v(C–O) bond of carboxylate groups coordinated to the iron centers of the MOF. The free ligand is also observed through the C=O stretching vibration band at 1704 cm^{-1}.

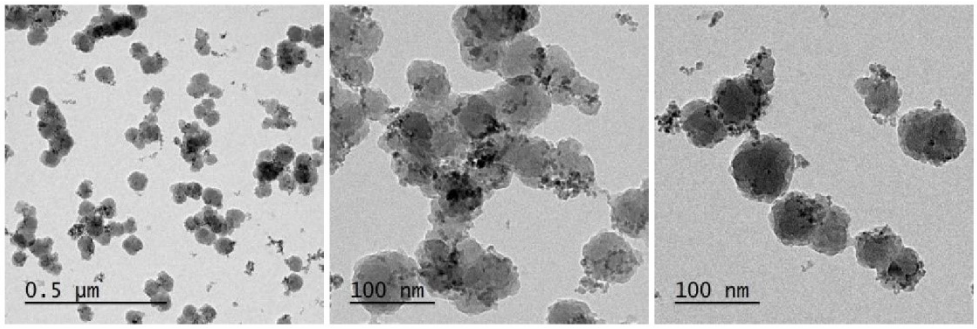

Figure S7. TEM images of USPIO(20)@MIL nano-objects.

6-Characterization of USPIO(10)@MIL nano-objects

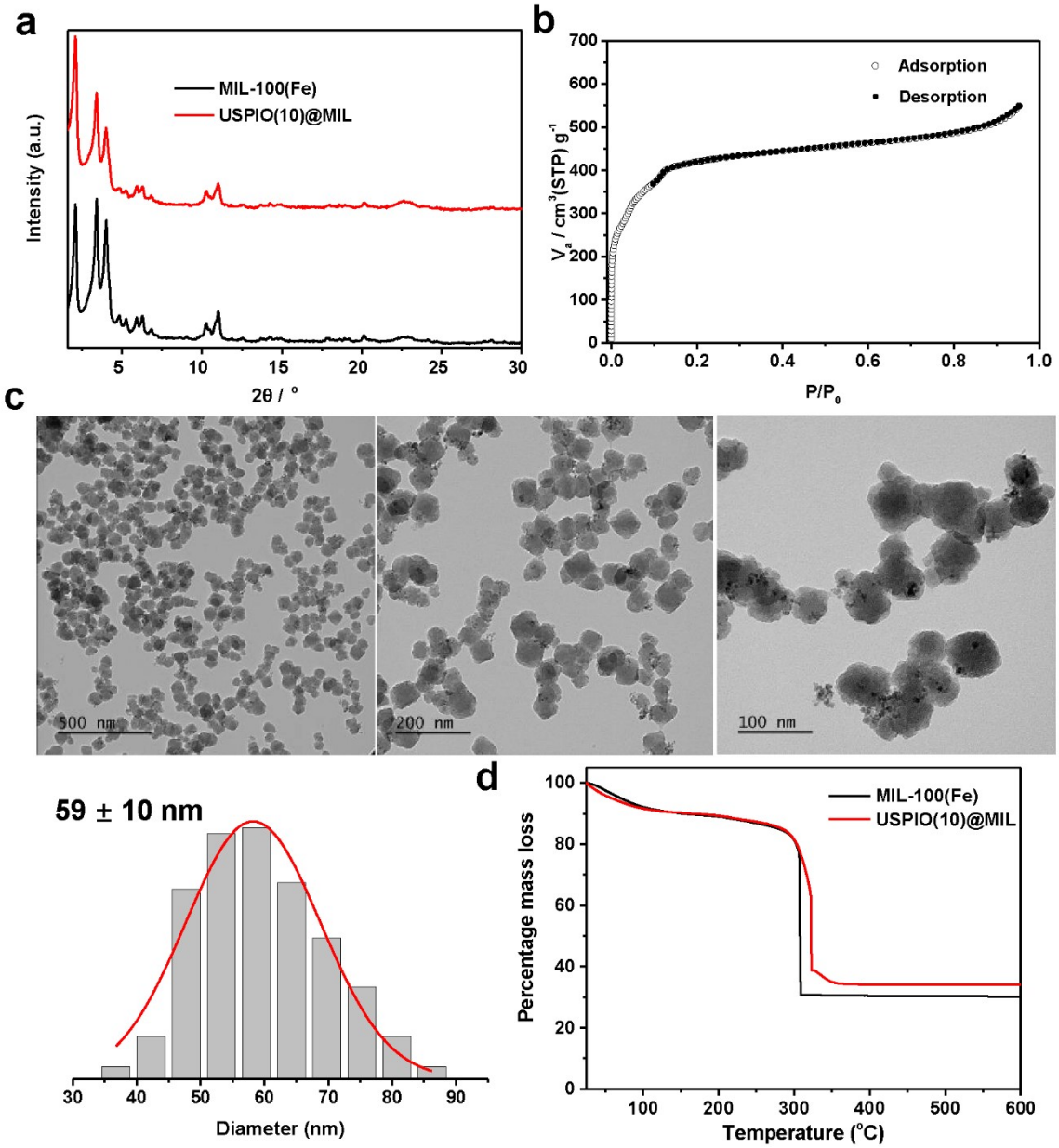

Figure S8. Characterizations of USPIO(10)@MIL: a) PXRD diagram; b) N_2 adsorption / desorption isotherms; c) TEM images; d) TGA.

The microstructure of USPIO(10)@MIL is close to that of USPIO(20)@MIL. The TEM images show that USPIO(10)@MIL consists of spheroidal particles of 59 ± 10 nm in diameter with a small diameter distribution.

7-Colloidal stability of MIL-100(Fe) and USPIO@MIL nano-objects

MIL-100(Fe) and USPIO(20)@MIL in EtOH were centrifuged and re-dispersed at a concentration of 200 µg/mL in different media: Milli Q water, 0.9% NaCl aqueous solution (Saline), PBS (pH7.4, 10 mmol·L^{-1}), PBS solution with 5.4% w/v bovine serum albumin (BSA), Dulbecco's Modified Eagle Medium (DMEM) and 90% DMEM + 10% fetal bovine serum (FBS). After sonication (10% amplitude for 30 seconds), the samples' hydrodynamic diameters were recorded over 3 experimental replicates. The Zeta potentials of MIL-100(Fe) and USPIO(20)@MIL in Mill Q water were also recorded.

Furthermore, the long term colloidal stability of USPIO(20)@MIL was studied by measuring the evolution of their diameter with time at 37 °C, in three different media to mimic the blood environment, namely Milli Q water, a pure neutral PBS solution and a PBS solution (10 mmol·L^{-1}) with 5.4% w/v BSA. Values of diameter and PdI were recorded over a period of 24h (289 runs, 10 measurements per run and 30 seconds per measurement).

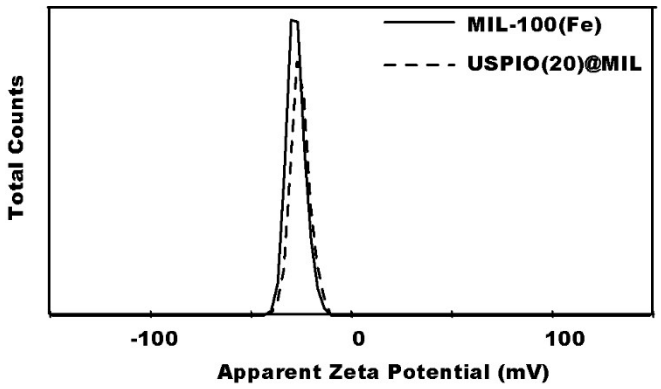

Figure S9. Measurements of zeta potentials of MIL-100(Fe) and USPIO(20)@MIL in Milli Q water. The values of zeta potential of MIL-100(Fe) and USPIO(20)@MIL are respectively equal to -28 ± 1 mV and -26 ± 1 mV.

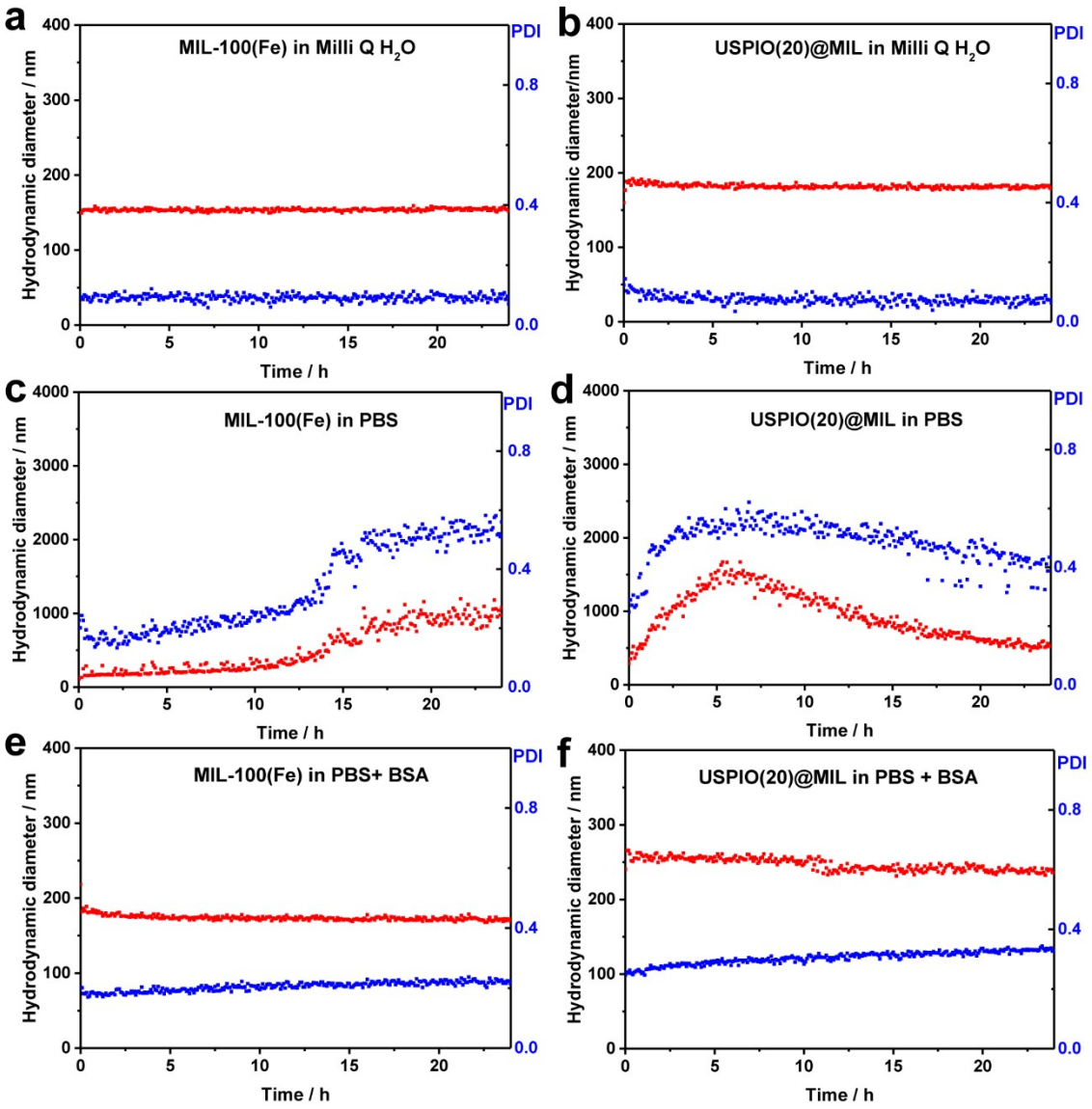

Figure S10. Evolution of the average particle diameter (by intensity) (red line) and polydispersity index (PdI) (blue line) of MIL-100(Fe) and USPIO(20)@MIL in (a-b) Milli Q water, (c-d) 10 mM PBS (pH7.4), (e-f) 10 mM PBS (pH7.4) + 5.4% w/v BSA over a time period of 24 h.

To confirm the impact of bovine serum albumin on the colloidal stability of USPIO(20)@MIL NPs, USPIO(20)@MIL NPs were redispersed into DMEM, 90% DMEM + 10% FBS and PBS solution (10 mmol·L^{-1}) at the pH of 5.1 and 6.5 with or without 5.4% w/v BSA, respectively. The average particle diameter was also monitored at regular interval for a period of 24 h.

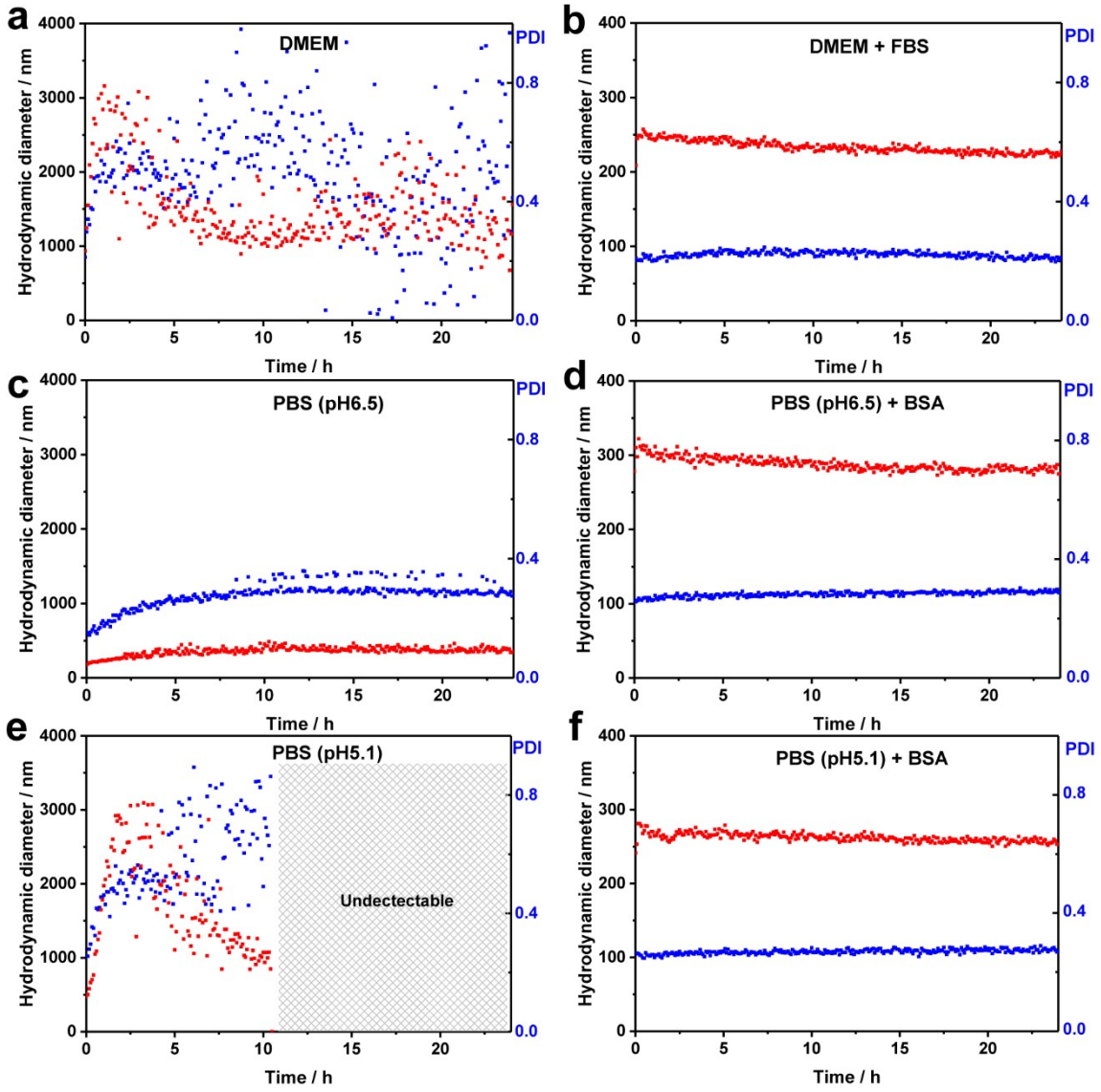

Figure S11. Evolution of the average particle diameter (by intensity) (red line) and polydispersity index (PdI) (blue line) of USPIO(20)@MIL in (a) DMEM, (b) 90% DMEM + 10% FBS, (c) 10 mM PBS (pH 6.5), (d) 10 mM PBS (pH 6.5) + 5.4% w/v BSA, (e) 10 mM PBS (pH 5.1) and (f) 10 mM PBS (pH 5.1) + 5.4% w/v BSA over a time period of 24 hours.

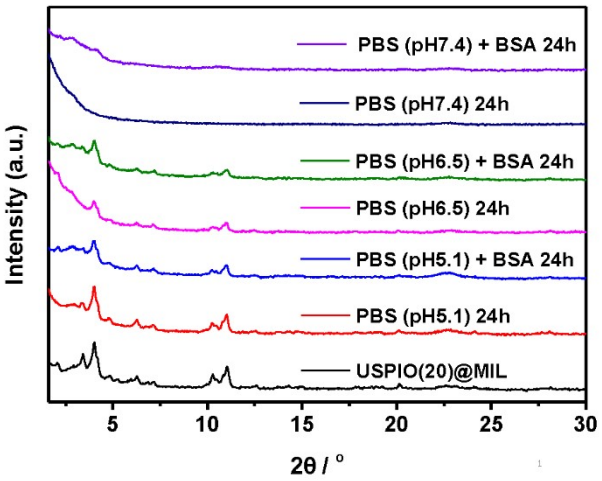

Figure S12. PXRD patterns of 1 mg/mL USPIO(20)@MIL NPs after mixing in 0.01M PBS (pH = 5.1, 6.5 and 7.4) with or without 5.4% w/v BSA at 37 °C for 24 hours.

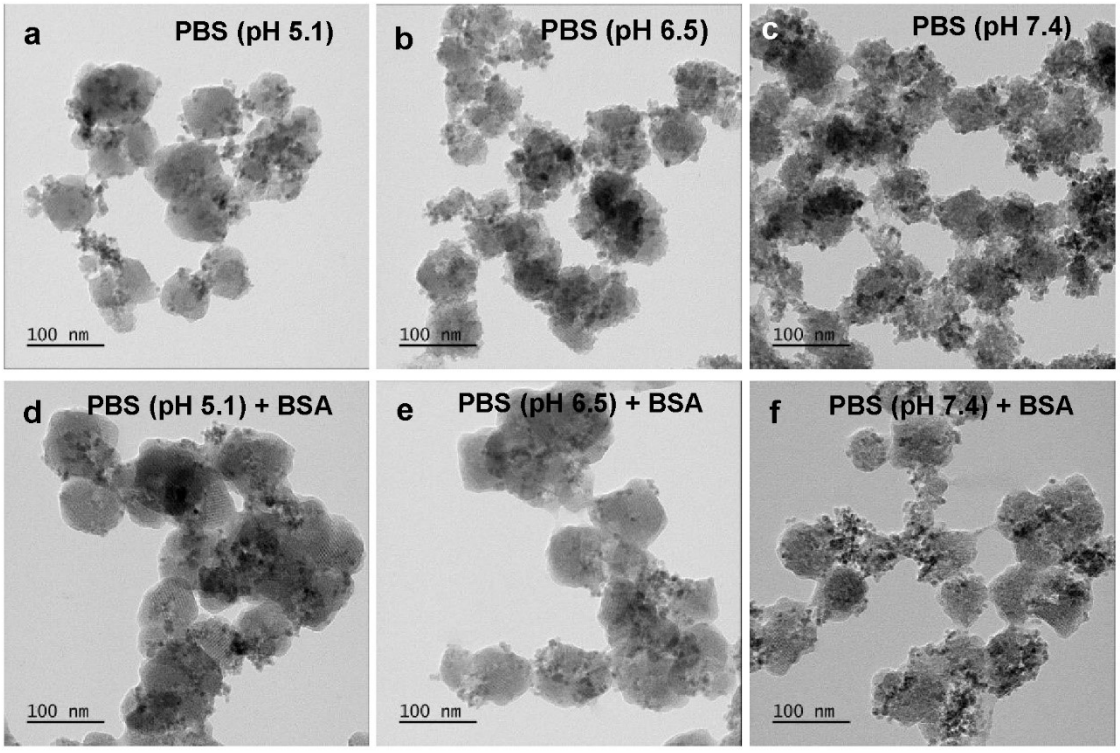

Figure S13. TEM observations of USPIO(20)@MIL NPs obtained after mixing in 0.01M PBS at the pH of (a, d) 5.1, (b, e) 6.5 and (c, f) 7.4 with or without 5.4% w/v BSA at 37 °C for 24 hours. The sample was washed in H_2O before TEM grid preparation.

8-^{57}Fe Mössbauer spectroscopy.

The ^{57}Fe Mössbauer spectra were obtained using a ^{57}Co/Rh γ-ray source, mounted on a conventional constant acceleration vibrating electromagnetic transducer. They were performed on a powdered sample containing about 15 mg of Fe at 300 and 77 K in a zero magnetic field and at 77 K under a 0.04 T magnetic field oriented perpendicular to the γ-beam. The calibration is obtained using a α-Fe foil and the values of isomer shift were referred to that of α-Fe at 300 K. After registration of a spectrum with a large velocity scale (not shown here), the spectrum at 300 K (Figure S14 top) results in only a quadrupolar feature which consists of an asymmetrical quadrupolar doublet: its description can be obtained by considering a quadrupolar spectrum (blue) corresponding to that of MIL-100(Fe) and a second quadrupolar component (red) attributed to γ-Fe_2O_3 NPs. Indeed, taking into account the diameter of γ-Fe_2O_3 NPs (7 ± 3 nm), they should exhibit fast superparamagnetic relaxation phenomena giving rise to a quadrupolar structure. Their respective proportions of both MIL-100(Fe) and γ-Fe_2O_3 are 66 and 34%, in rather fair agreement with the quantification by HPLC / ICP-MS (69-31%). At 77 K, as shown in Figure S14 (middle), a part of the quadrupolar structure splits into a magnetic sextet composed of broadened and asymmetrical lines. In addition to the central quadrupolar feature corresponding to the MIL-100(Fe) component, the magnetic sextet assigned to γ-Fe_2O_3 NPs was described by means of a hyperfine field distribution. The 69 and 31% proportions estimated at 77 K are fully consistent with the experimental values (the small disagreement at 300 K is due to the small difference in the Lamb-Mössbauer factors characteristics of the two phases). The presence of non-interacting γ-Fe_2O_3 NPs cannot be clearly excluded and it is not possible to distinguish the aggregated γ-Fe_2O_3 NPs at the surface of USPIO(20)@MIL and those located in the core of USPIO(20)@MIL (see Figure S14 bottom).

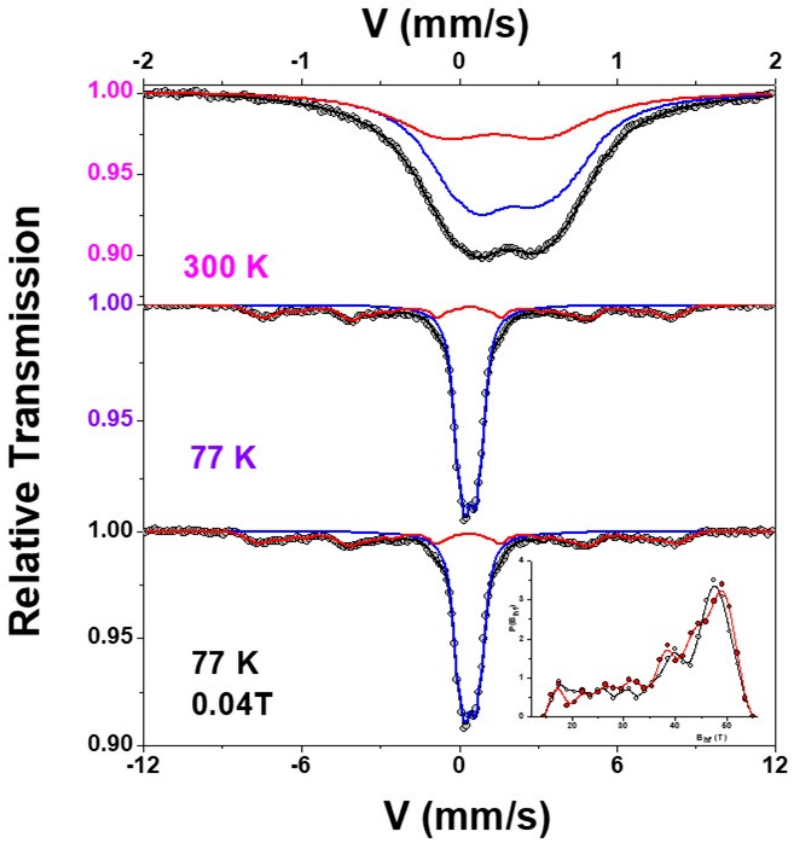

Figure S14. ^{57}Fe Mössbauer spectra of USPIO(20)@MIL recorded at 300 K(top) and 77 K (middle) in a zero magnetic field and at 77 K under a 0.04 T magnetic field.

9-Cellular uptake of USPIO(20)@MIL by RAW 264.7 macrophages

Synthesis of USPIO(20)@MIL/RhB. To observe the cellular uptake of USPIO(20)@MIL, USPIO(20)@MIL was loaded with a fluorescent dye Rhodamine B (RhB). Typically, 1 mL RhB stock solution (1mg/mL) was first diluted in 4 mL Milli Q water, then added to 5 mg of USPIO(20)@MIL and kept stirring at 600 rpm for 24 h with the protection of tin foil. The resulting USPIO(20)@MIL/RhB nanoparticles were collected by centrifugation and washed with Milli Q water to remove the free RhB. Then, the final product was redispersed in 5 mL Milli Q water with tin foil covering and kept in 4 ^{o}C fridge until use.

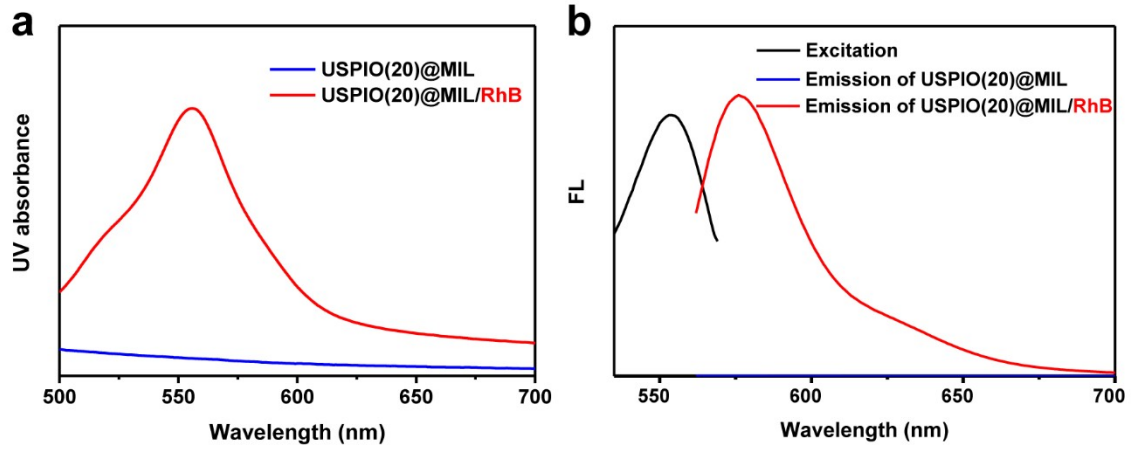

Figure S15. a) UV-vis spectra of USPIO(20)@MIL and USPIO(20)@MIL/RhB, (b) Fluorescence emission spectra of USPIO(20)@MIL and USPIO(20)@MIL/RhB (λ_{em}= 576 nm).

While the bare USPIO(20)@MIL NPs do not display any absorbance peak in the visible spectrum, USPIO(20)@MIL/RhB NPs present one peak at 550 nm. Moreover, USPIO(20)@MIL/RhB NPs present fluorescence properties (λ_{em} = 576 nm) by excitation with visible light while the USPIO(20)@MIL NPs do not exhibit any fluorescence properties.

Cell Culture

RAW 264.7 macrophage cells (and Hela cells) were cultured in high glucose Dulbecco's Modified Eagle Medium (DMEM) containing 10% FBS and 1% penicillin and streptomycin at 37 ^{o}C in a humidified 5% CO_2 atmosphere.

Cellular uptake study by confocal laser scanning microscopy and ICP-MS

The cellular uptake of the USPIO(20)@MIL was evaluated by CLSM and ICP-MS on RAW 264.7 macrophages. Cells were seeded into 6-well plate (2×10^5 cells/well) and maintained overnight. The DMEM/FBS 10% medium was then replaced with 2 mL of DMEM/FBS 10% medium containing USPIO(20)@MIL/RhB (50 $\mu g \cdot ml^{-1}$), followed by an incubation at 37 ^{o}C for 1 h, 2 h, 4 h, 6 h and 8 h. As for CLSM, after the removal of the MOF containing media, RAW 264.7 cells were washed with PBS for three times. Then the as prepared samples were imaged by CLSM (ZEISS LSM780, Germany). The laser excitation wavelength is 543 nm.

In parallel, the quantification of the cellular uptake of USPIO(20)@MIL in RAW 264.7 cells was performed through the quantification of the intracellular iron content by ICP-MS. The same incubation procedure was performed. After incubation, the RAW 264.7 cells were washed with PBS (pH 7.4), then trypsinized, harvested by centrifugation (1000 rpm, 5 min). Subsequently, after washing again with PBS, the pellet was treated with 1mL of concentrated nitric acid overnight. The resulting sample solution was further diluted with 2% nitric acid, prior to the quantification of iron by ICP MS. These experiments were performed in triplicate.

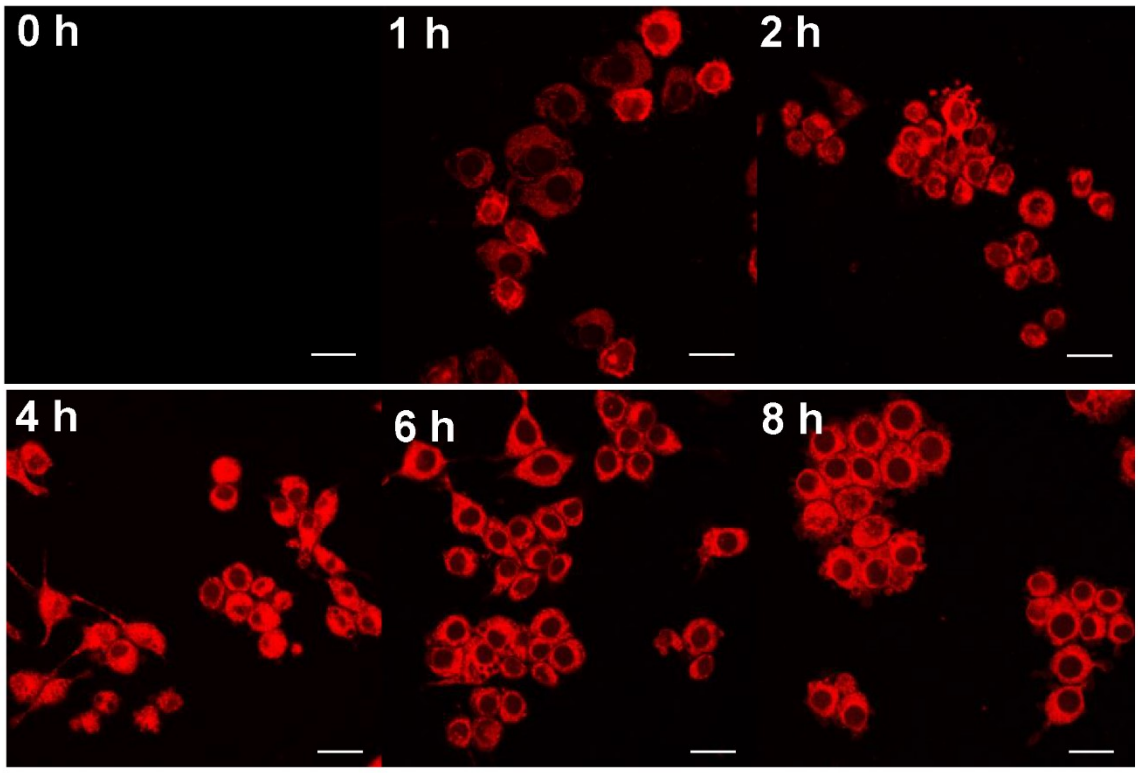

Figure S16. Internalization of Rhodamine-labeled USPIO(20)@MIL in RAW 264.7 macrophages as shown by CLSM (Scale bar = 20 μm).

TEM of cells.

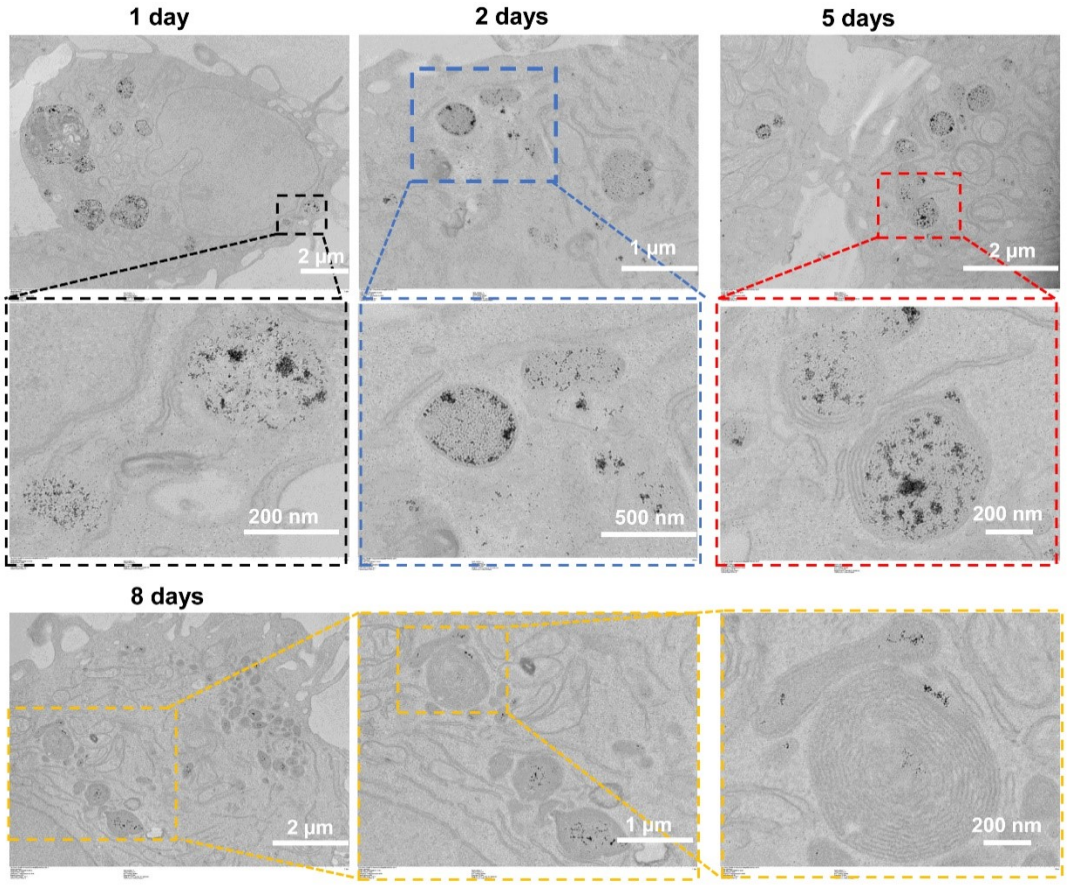

Figure S17. 2D TEM slices images of RAW 264.7 cells at different times (1 day, 2, 4 or 8 days) after incubation with USPIO(20)@MIL (50 µg·mL^{-1}) for 24 h.

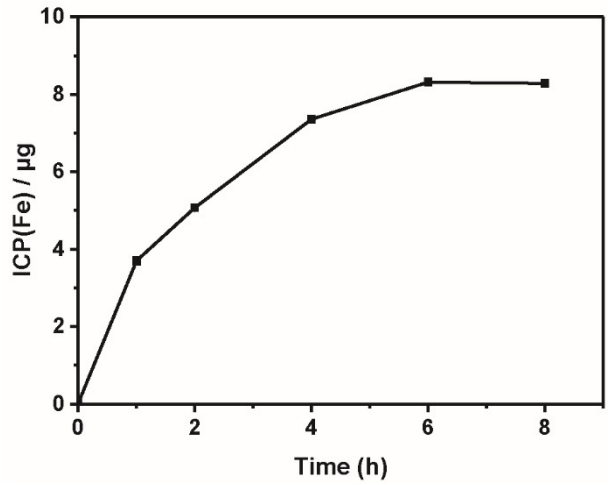

Figure S18. Quantification of the intracellular Fe^{3+} as a function of the incubation time of RAW 264.7 macrophages with USPIO(20)@MIL NPs. These experiments were performed in triplicate.

10-Encapsulation and release of methotrexate

Encapsulation of methotrexate in USPIO(20)@MIL

Firstly, 30 mg of MTX was totally dissolved in 30 mL 10 mM HCl solution with foil wrap, after stirring at 200 rpm under 55°C in the incubator for 1 hour. Then 30 mg of MIL-100(Fe) or USPIO(20)@MIL was dispersed in the prepared MTX solution (1 $mg \cdot mL^{-1}$). Other weight ratios (1:0.25, 1:0.5 and 1:2) of MOFs to MTX were also studied. The resulting suspension was stirred at 200 rpm under 37 °C overnight. The MTX loaded MIL-100(Fe) and USPIO(20)@MIL nano-objects (*i.e.* MIL-100(Fe)/MTX or USPIO(20)@MIL/MTX NPs) were washed with 10 mM HCl three times. The loading capacity of MIL-100(Fe) or USPIO(20)@MIL was determined in triplicate by UV-Vis spectrophotometer at 306 nm (maximum absorbance wavelength of MTX) and HPLC. The mobile phase of HPLC is 25:75 v/v methanol: ammonium acetate buffer (0.05 $mol \cdot L^{-1}$, pH 6.0). A flow rate of 1 $mL \cdot min^{-1}$ and a sample injection volume of 25 µL were used during all analyses. Then, the present of loading capacity (LC) or entrapment efficiency (EE) was calculated using the following equation:

LC = (Mass of total drug - Mass of free drug) / Mass of total MOF

EE = (Mass of total drug - Mass of free drug) / Mass of total drug

MTX release of USPIO(20)@MIL/MTX

Typically, after the loading of MTX (MOF : MTX = 1:1), USPIO(20)@MIL/MTX HCl solution (1 $mg \cdot mL^{-1}$) was divided into 1.5 mL aliquots and after an extra centrifuge/redisperse step, the cumulative release behavior of MTX from USPIO(20)@MIL/MTX (1 $mg \cdot mL^{-1}$) was investigated in PBS (pH 5.1 and pH 7.4) with or without GSH for different times (0.5 h, 1 h, 4 h, 8 h, 24 h, 48 h and 72 h). At different time intervals, the suspension of USPIO(20)@MIL/MTX was centrifuged (13400 rpm, 15 min) and 0.5 mL of the release

medium was replaced by the same volume of fresh medium. The concentration of released MTX and ligand BTC (in PBS) was measured in triplicate by HPLC. The release ferric ions was investigated by ICP-MS. Similarly, the release of MTX in DMEM and DMEM + 10% FBS from USPIO(20)@MIL/MTX also was monitored by HPLC and measured in triplicate.

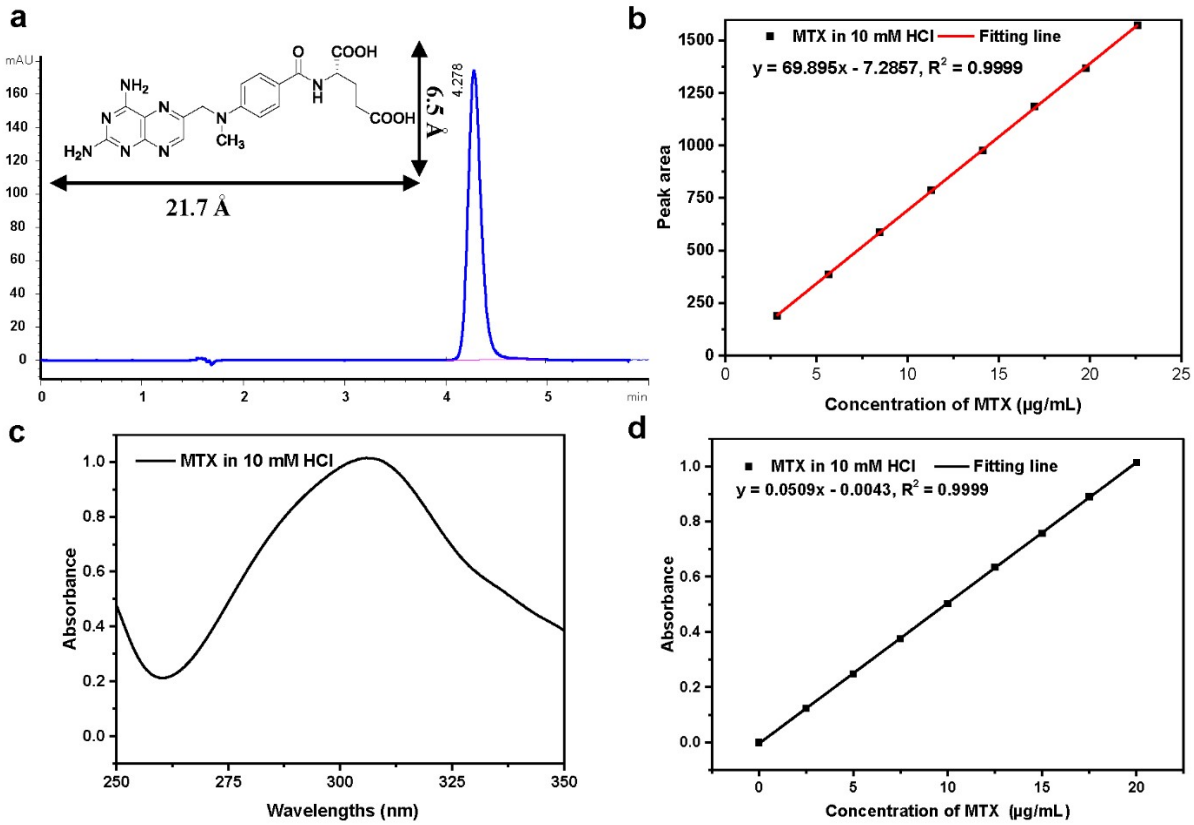

Figure S19. a) HPLC chromatogram of MTX (Inserted: Molecular structure of MTX); b) MTX calibration curves in 10 mM HCl by HPLC; c) UV-Vis spectrum of MTX; d) MTX calibration curves in 10 mM HCl by UV-Vis.

Table S2. MTX loading capacity (LC) or entrapment efficiency (EE) of MIL-100(Fe) and USPIO(20)@MIL. Each LC and EE value was determined in triplicate.

Weight Ratio (MOF : MTX)	**MIL-100(Fe)/MTX** LC (%)	EE (%)	**USPIO(20)@MIL/MTX** LC (%)	EE (%)
1:0.25	25 ± 0.01	99 ± 0.05	25 ± 0.04	99 ± 0.2
1:0.5	46 ± 0.03	92 ± 0.05	43 ± 0.05	86 ± 0.1
1:1	60 ± 1	60 ± 1	47 ± 3	47 ± 3
1:2	61 ± 5	30 ± 3	46 ± 10	23 ± 5

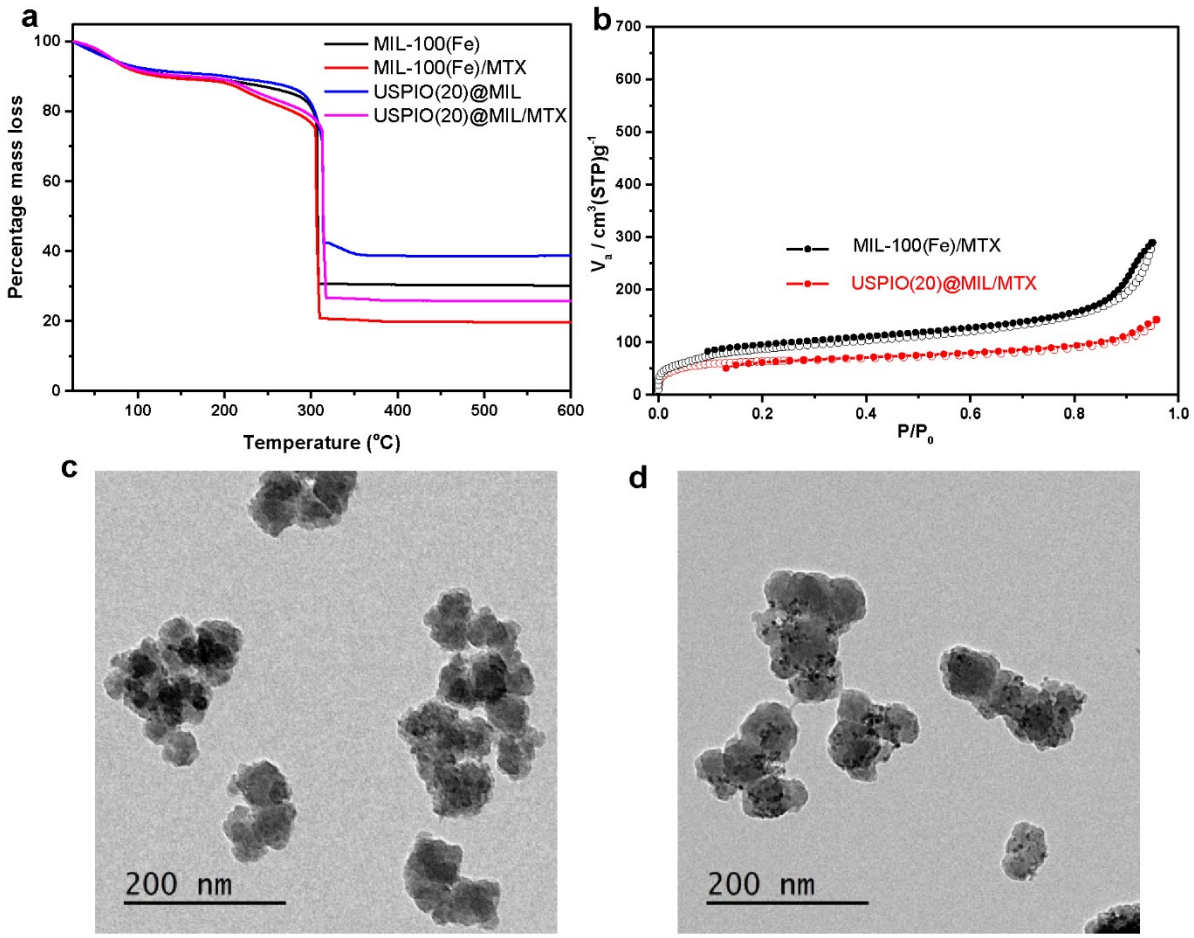

Figure S20. a) TGA and (b) N_2 adsorption / desorption isotherms of MIL-100(Fe)/MTX and USPIO(20)@MIL/MTX. TEM images of (c) MIL-100(Fe)/MTX and (d) USPIO(20)@MIL/MTX.

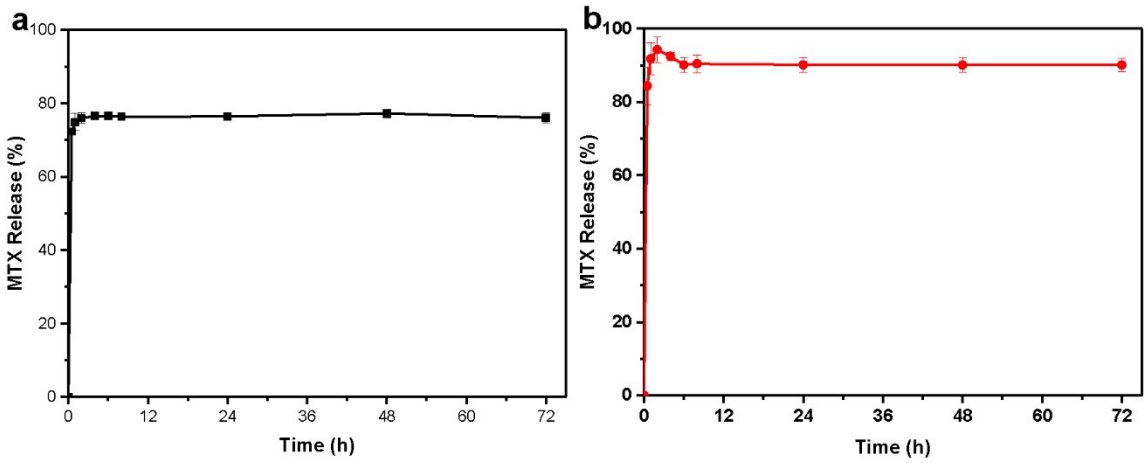

Figure S21. MTX release in (a) DMEM and (b) DMEM + 10% FBS from USPIO(20)@MIL/MTX by HPLC.

11-Encapsulation and release of doxorubicin.

Encapsulation of doxorubicin in USPIO(20)@MIL

5 mg of USPIO(20)@MIL was dispersed in 1.5 mL of Dox solution (10 mg/mL, Milli-Q water). The resulting suspension was stirred at 200 rpm at 37 ^{o}C for 24 h. The Dox loaded USPIO(20)@MIL nano-objects (*i.e.* USPIO(20)@MIL/Dox) were washed with Mill-Q water three times. The loading capacity of USPIO(20)@MIL/Dox was determined in triplicate by UV-Vis spectrophotometer at 480 nm (maximum absorbance wavelength of Dox).

Doxorubicin release of USPIO(20)@MIL/Dox

The cumulative release behaviour of Dox from USPIO(20)@MIL/Dox (1mg/mL, 1.5 mL) was investigated in PBS (pH 5.1 and pH 7.4) with or without GSH for different times (0.5 h, 1 h, 4 h, 8 h, 24 h, 48 h and 72 h). At different time intervals, the suspension of USPIO(20)@MIL/Dox was centrifuged (13400 rpm, 15 min) and 0.5 mL of the release medium was replaced by the same volume of fresh medium. The concentration of released Dox (in PBS) was measured in triplicate by UV-Vis spectrophotometer. The release of ligand BTC and ferric ions were investigated by HPLC and ICP-MS, respectively. Similarly, the release of Dox from MIL-100(Fe) and USPIO(20)@MIL/Dox was also studied in phenol red free DMEM (for UV-Vis detection).

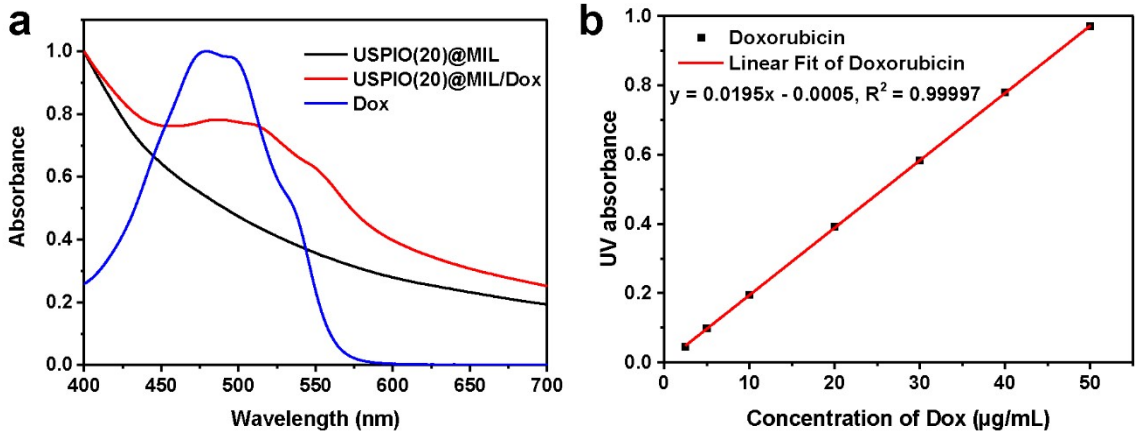

Figure S22. a) Normalized UV-Vis spectra of USPIO(20)@MIL, USPIO(20)@MIL/Dox and Dox. b) Calibration curve of Doxorubicin in water by UV-Vis spectroscopy.

Table S3. Dox loading capacity (LC) or entrapment efficiency (EE) of MIL-100(Fe) and USPIO(20)@MIL. Each LC and EE value was determined in triplicate.

Weight Ratio	**MIL-100(Fe)/Dox**		**USPIO(20)@MIL/Dox**	
(MOF : Dox)	LC(%)	EE(%)	LC(%)	EE(%)
1 : 0.25	24.96 ± 0.01	99.8 ± 0.01	24.85 ± 0.01	99.39 ± 0.04
1 : 0.5	48.3 ± 0.4	96.6 ± 0.8	43.4 ± 0.5	86.8 ± 1
1 : 1	57.3 ± 0.6	57.3 ± 0.6	48.4 ± 1.6	48.4 ± 1.6
1 : 3	55.8 ± 0.5	18.6 ± 0.2	49.9 ± 4.3	16.6 ± 1.4

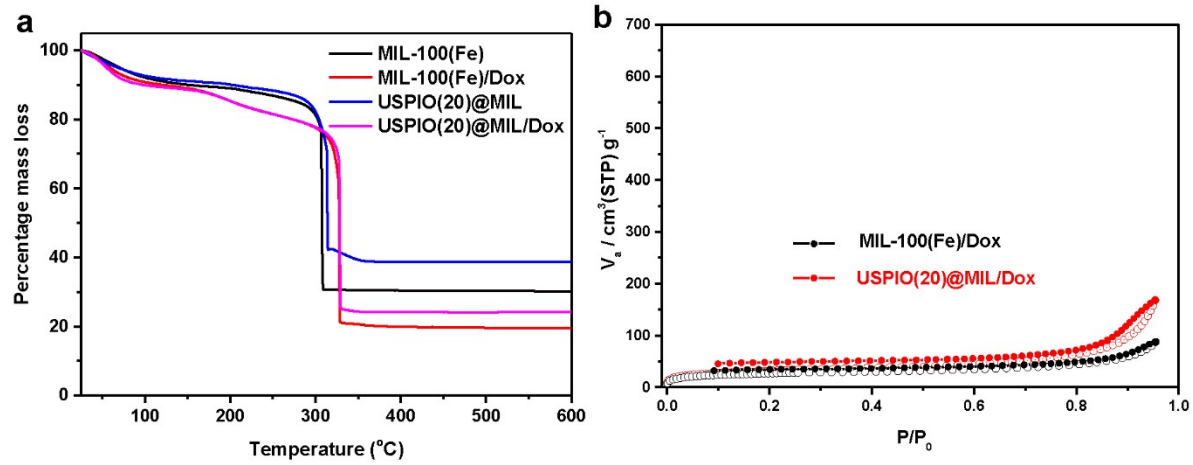

Figure S23. a) TGA and (b) N_2 adsorption/desorption isotherms of MIL-100(Fe)/Dox and USPIO(20)@MIL/Dox.

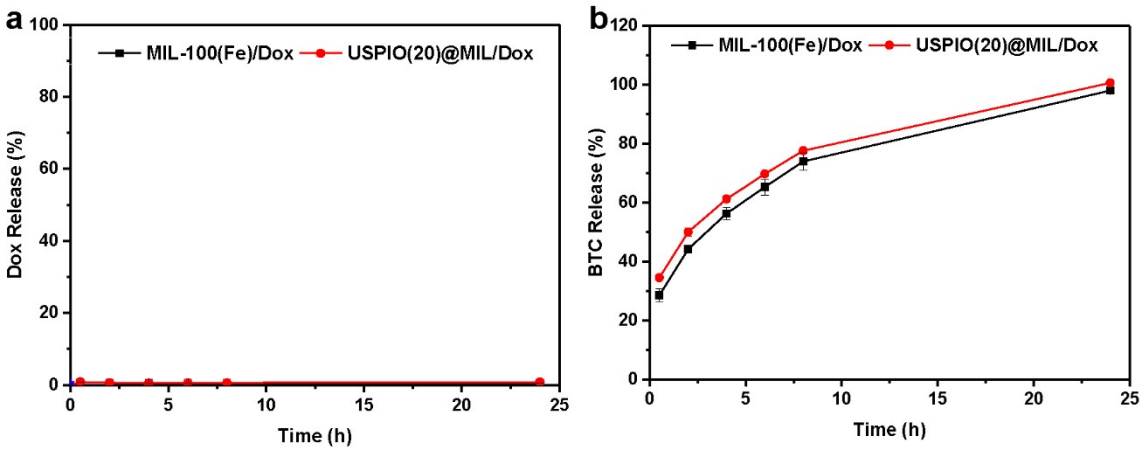

Figure S24. a) Dox and (b) BTC release of MIL-100(Fe)/Dox and USPIO(20)@MIL/Dox in phenol-free DMEM.

12-*In vitro* cytotoxicity assay of MIL-100(Fe), USPIO(20)@MIL, USPIO(20)@MIL/MTX and USPIO(20)@MIL/Dox against normal RAW 264.7 macrophages and Hela cells

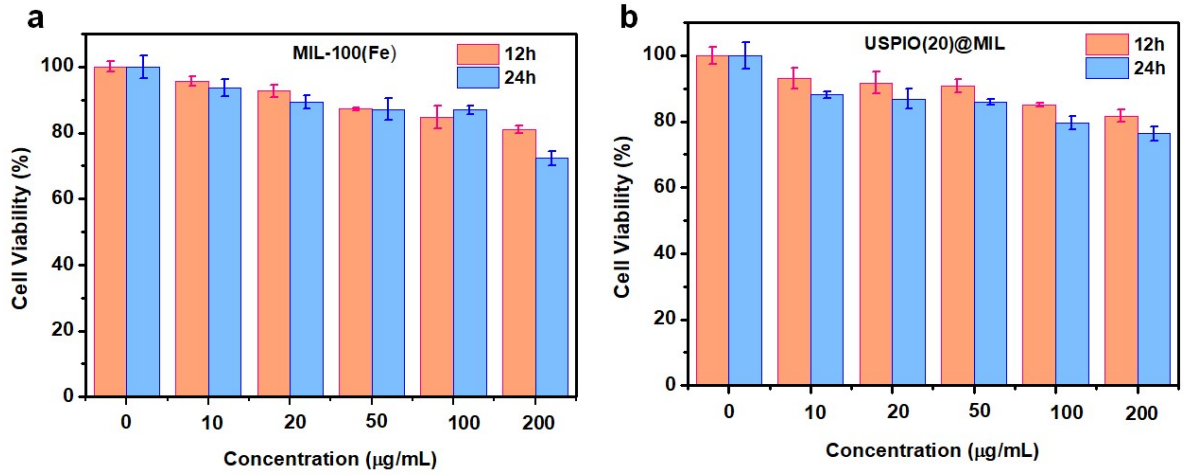

Figure S25. Normalized Hela cells viability obtained after incubation with (a) MIL-100(Fe) and (b) USPIO(20)@MIL at different concentrations for 12 and 24 h. The experimental data were determined in triplicate.

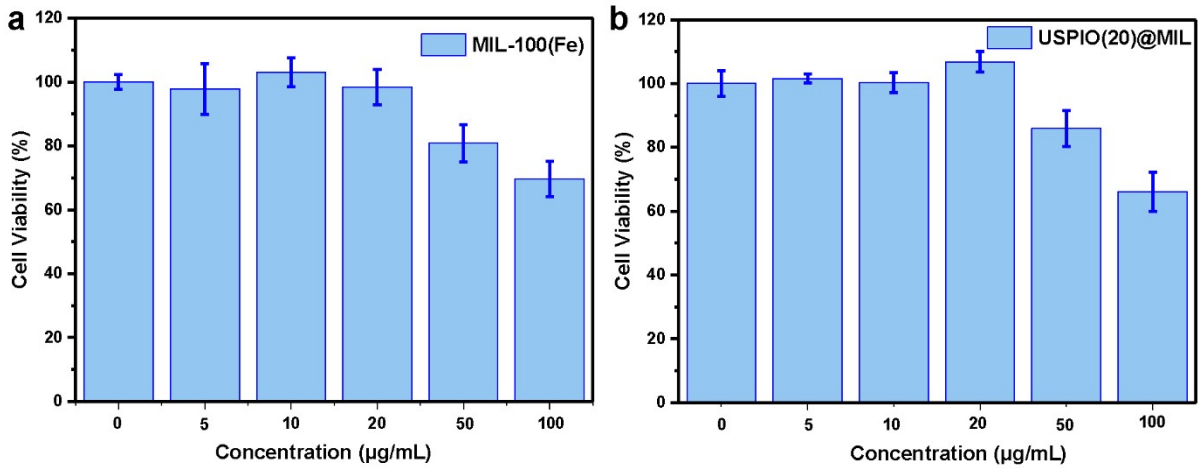

Figure S26. Normalized cell viability of RAW 264.7 macrophages after incubation with (a) MIL-100(Fe) and (b) USPIO(20)@MIL for 24 h. The experimental data were determined in triplicate.

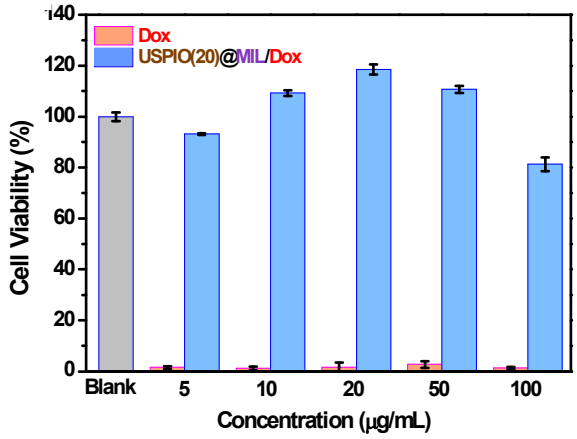

Figure S27. Cell viability of RAW 264.7 macrophages exposed for 24 h to USPIO(20)@MIL/Dox and equivalent free Dox of different concentrations. The experimental data were determined in triplicate.

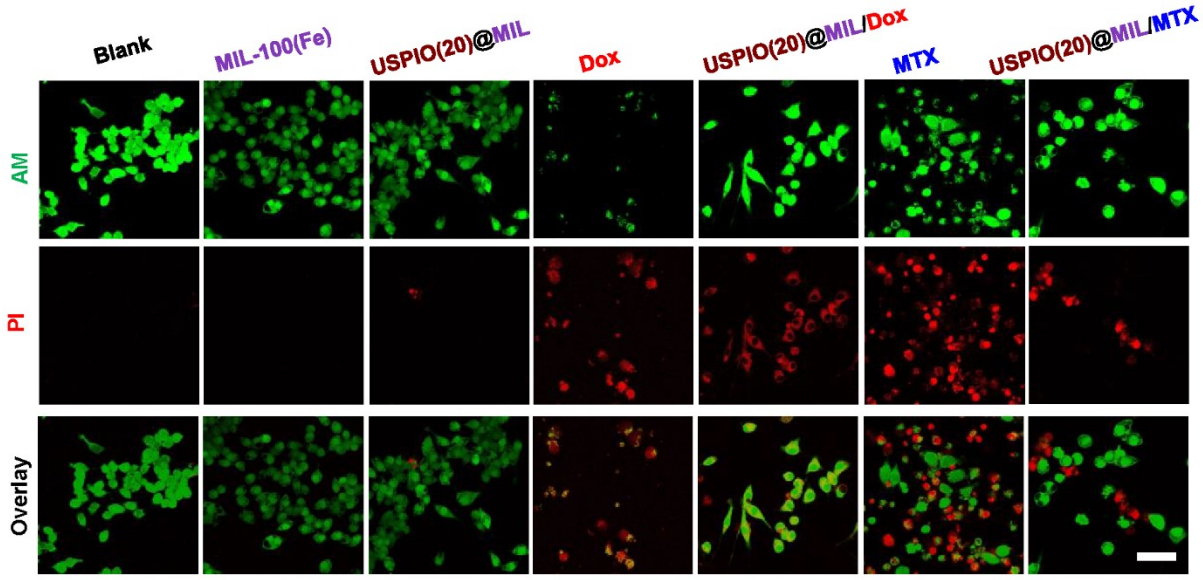

Figure S28. AM/PI staining of normal RAW 264.7 macrophages after co-culture with MIL-100(Fe), USPIO(20)@MIL, Dox, USPIO(20)@MIL/Dox, MTX and USPIO(20)@MIL/MTX for 24 h. Live & dead cells were stained by green and red, respectively. [MIL-100(Fe)] = 40 $\mu g \cdot mL^{-1}$, [USPIO(20)@MIL] = 50 $\mu g \cdot mL^{-1}$, [Dox] = 25 $\mu g \cdot mL^{-1}$, [USPIO(20)@MIL/Dox] = 50 $\mu g \cdot mL^{-1}$, [MTX] = 23 $\mu g \cdot mL^{-1}$ and [USPIO(20)@MIL/MTX] = 50 $\mu g \cdot mL^{-1}$. Scale bar = 50 μm. The experimental data were determined in triplicate.

13-Anti-inflammatory capacity of USPIO(20)@MIL/MTX and USPIO(20)@MIL/Dox

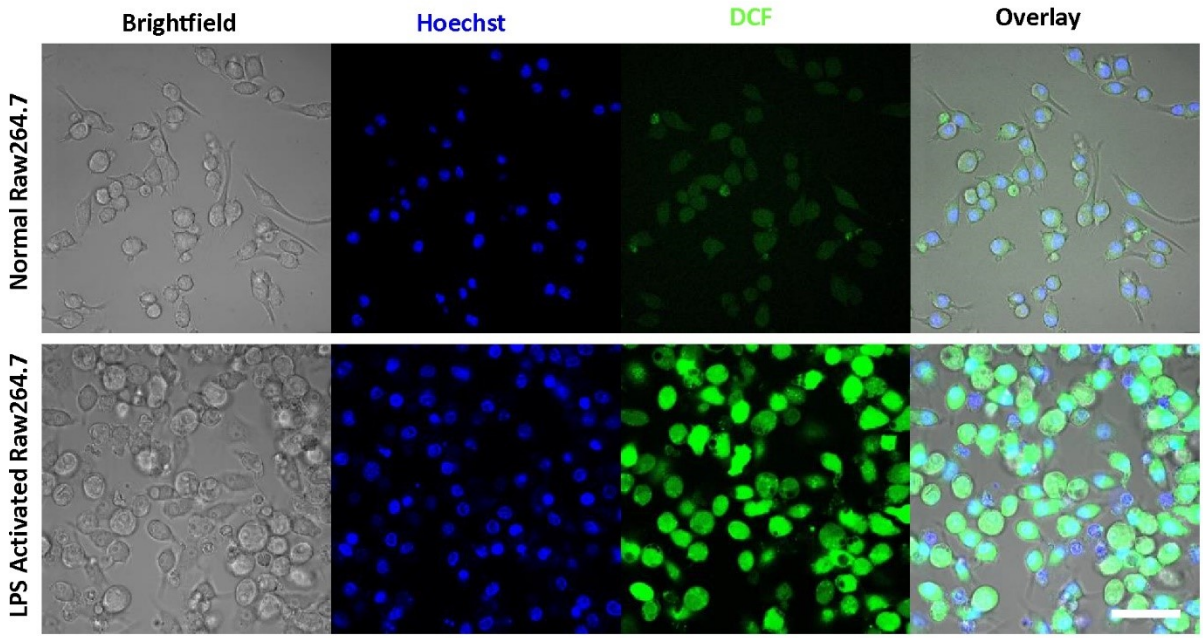

Figure S29. *In vitro* ROS (DCF fluorescence) imaging on normal RAW 264.7 cells and LPS activated RAW 264.7 cells and Hoechst as a nucleus staining dye. Scale bar = 50 µm.

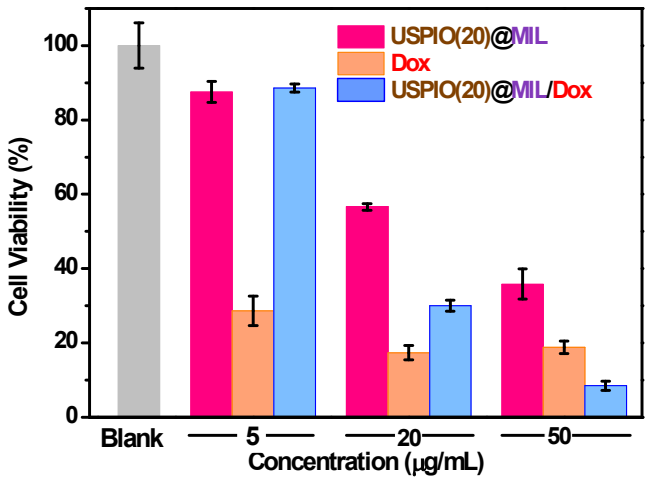

Figure S30. Cell viability of LPS activated RAW 264.7 macrophages incubated with different concentrations of USPIO(20)@MIL (5, 20 and 50 $\mu g \cdot mL^{-1}$), USPIO(20)@MIL/Dox and equivalent free Dox (2.5, 10 and 25 $\mu g \cdot mL^{-1}$) for 24h. The experimental data were determined in triplicate.

14-Evaluation of the concentrations of pro-inflammatory cytokines by enzyme-linked immunosorbent assay (ELISA) assays

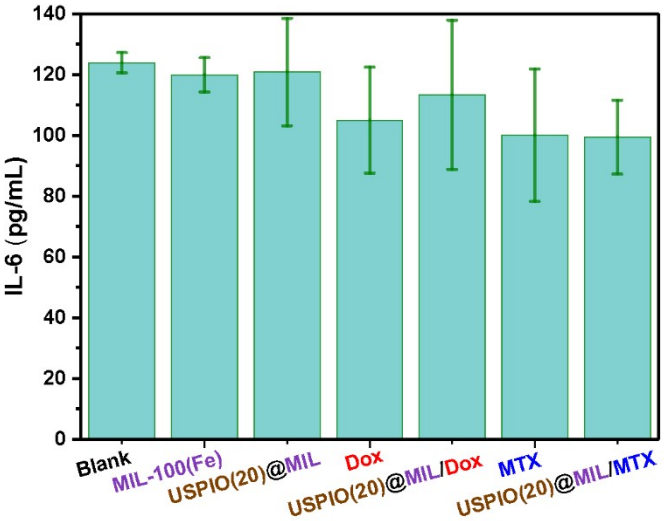

Figure S31. The concentrations of the inflammatory cytokines IL-6 in cell culture media after the treatment of different formulations ([MIL-100(Fe)] = 4 μg·mL^{-1}, [USPIO(20)@MIL] = 5 μg·mL^{-1}, [Dox] = 0.25 μg·mL^{-1}, [USPIO(20)@MIL/Dox] = 5 μg·mL^{-1}, [MTX] = 2.3 μg·mL^{-1}, [USPIO(20)@MIL/MTX] = 5 μg·mL^{-1}) for 24 h. Note that the concentration of Dox here was ten times lower than the loaded Dox of USPIO(20)@MIL/Dox to limit its toxicity. Results are shown as mean ± SD. The experimental data were determined in triplicate.

15-Cytotoxicity of USPIO(20)@MIL/Dox against Hela cells

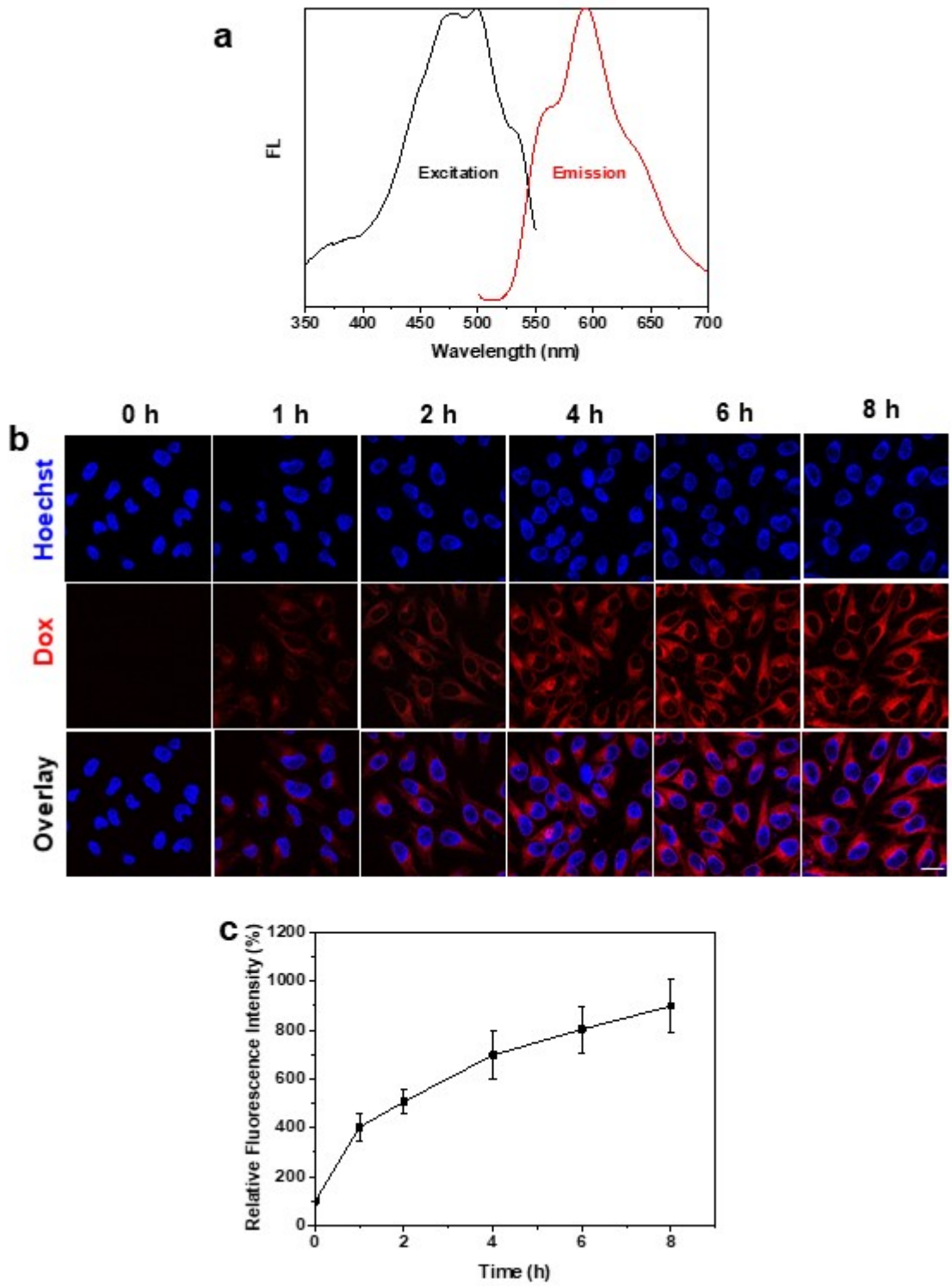

Figure S32. a) Excitation and fluorescence spectra of USPIO(20)@MIL/Dox in water. b) Internalization of USPIO(20)@MIL/Dox in Hela cells as shown by CLSM (Scale bar = 10 µm) and (c) quantification of the intracellular relative fluorescence intensity of Dox as a function of the incubation time of Hela cells with USPIO(20)@MIL NPs.

16-Relaxometry and magnetic properties of USPIO@MIL nano-objects.

Relaxivity measurements

The T_2 relaxation time were measured in 4.7 T field strength. For each type of sample (USPIO(20)@MIL, USPIO(10)@MIL, MIL-100(Fe) and γ-Fe_2O_3), a stock solution was prepared in physiological conditions at pH 7.5 with PBS solution at 0.02 mol·L^{-1} and 5.4% w/v BSA. Two-fold serial dilutions were then performed in the same medium and 7 aliquots of 800 µL were then prepared for T2 measurements with iron concentrations ranging from ~ 8.56 to 0.01 mM. The Fe content was then determined using a NexloN 300X ICP-MS (PerkinElmer, Waltham, MA, U.S.A.). Samples were digested in 5 M HNO_3 solution for 24 h before their dilution in 2% HNO_3 for quantitative analysis. Standard calibration curve was performed using a series of Fe standard solution (5 to 100 ppb). T_2 relaxation time experiments were performed on a 4.7 T Bruker Biospec system (Ettlingen, Germany) equipped with a birdcage resonator for radio-frequency excitation and signal reception. T_2 measurements were performed at 25 °C with a CPMG (Carr–Purcell–Meiboon–Gill) imaging sequence (TR, 5000 or 10000 ms; inter echo-time, 5 ms; number of echo images, 256; FOV, 50 × 50 mm; matrix, 128 × 128; slice thickness, 2 mm). Relaxation data were analyzed with home-made software developed on Igor Pro (Wavemetrics, Lake Oswego, OR, USA). For each sample, the time evolutions of the magnetization were fitted according to mono-exponential functions. Relaxation rate R_2 (= $1/T_2$) was reported as a function of iron concentration to determine the relaxivity rate (r_2) of each sample.

Table S4. Relaxivity r_2 values of iron oxide NPs per mM Fe^{3+}

NPs/nano-objects	Relaxivity r_2[a] ($mM^{-1}.s^{-1}$)	Hydrodynamic diameter of nano-object (nm)	Surface modification	Reference
γFe_2O_3	171 ± 10	7 (3)	-	This paper
MIL-100(Fe)	3 ± 1	38 (7)	-	This paper
USPIO(20)@MIL	93 ± 2	49(10)	-	This paper
USPIO(10)@MIL	38 ± 2	49(10)	-	This paper
MIL/USPIO-cit (10)	93 ± 4	163 (77)	Citrate	[1]
MIL/USPIO-cit(1)	21 ± 2	155 (40)	Citrate	[1]
γ-Fe_2O_3	205	13	citrate	[2]
γ-Fe_2O_3	133	16	PAA_{2k}[b]	[2]
γ-Fe_2O_3	69.8/86.5	9	PAA_{2k} [b]	[2]
γ-Fe_2O_3	70	8	DMSA[c]	[2]
γ-Fe_2O_3	145	15	dextran	[2-3]
Endorem®	100	228-80	dextran	[4-5]
Sinerem®	90	50	-	[4]
Fe_3O_4 /ZIF-8-Au_{25}	35.49	-	-	[6]
Fe_3O_4-ZIF-8	372	-	-	[7]
PEG-NH_2@Fe_3O_4-ZIF-8	25.25	97 (8)	-	[8]
FePt-MOF	27.1	-	-	[9]
MIL-S	13.53	60	-	[10]
MIL-M	31.28	350	-	[10]
MIL-L	50.80	730	-	[10]
Fe_3O_4@C@MIL-100(Fe)	352.45	-	-	[11]
USPIO/MIL-101(Fe)-NH_2	170.96	450	-	[12]

[a]r_2 values per mM Fe^{3+}; [b]PAA_{2k}: poly(sodium acrylate); [c]DMSA: Dimercapto-succinic acid

Characterization of the magnetic properties

Nano-objects were dispersed in a PVA matrix and dried in a cylindrical Teflon mold. The magnetic moment of the samples was measured by a Quantum Design vibrating sample magnetometer (VSM) operating at a vibrating frequency of 40 Hz, with an integration time of 1 s. Calibration was performed on a high purity nickel sample with the same dimensions as the samples. Blank samples of a PVA matrix and of MIL-100(Fe) dispersed in PVA showed only

a linear dependence of magnetic moment with applied field and no superparamagnetic contribution; magnetic curves were analyzed after subtraction of the linear component. The magnetic moment of a single particle was obtained by Langevin fit of the experimental data with a fitting error less than 1%. The magnetization of a single particle was calculated using the effective diameter of the γ-Fe_2O_3 particles. Finally, the overall accuracy can be safely estimated as 10%.

Thermal variation of the zero-field cooled and field cooled (ZFC-FC) magnetization at H = 16 kA/m (*i.e.* 200 Oe) reveals superparamagnetism at room temperature for USPIO(20)@MIL and USPIO(10)@MIL nano-objects. Furthermore, the ZFC-FC curve of USPIO(20)@MIL shown in Figure S33 is similar to that of well-dispersed bare γ-Fe_2O_3 NPs measured in the same conditions.[1] The similarities lie in the steepness of the low temperature FC curve and the ZFC maximum temperatures which are 54 K and 52 K for USPIO@MIL and well dispersed bare γ-Fe_2O_3 NPs respectively.[13] The saturation magnetization at T = 300 K was obtained from the magnetic moment of each sample measured while the applied field was cycled. The magnetic field was driven above the saturation field which was 1.5×10^6 A/m (*i.e.* 20 kOe) for USPIO@MIL samples. For all measured samples, the magnetization was fully reversible upon magnetic field cycling. The coercive fields H_{coer} were below the detection limit which was 1.6 kA/m (*i.e.* 20 Oe). Both H_{coer} and T_{max} are consistent with an assembly of N quasi-independent particles and the Langevin model was applied at room temperature to get the saturation magnetization M_{sat} of the USPIO:

$$m(H) = M_{sat} \int_0^{\infty} N(D) \frac{\pi D^3}{6} \left(\tanh^{-1}(x) - \frac{1}{x} \right) \mathrm{d}D, \quad x = M_{sat} \frac{\pi D^3}{6} \frac{\mu_0 H}{k_B T},$$

where N(D) is the number of USPIO having the diameter D, T is the temperature, k_B the Boltzmann constant and μ_0 the magnetic induction of the vacuum.

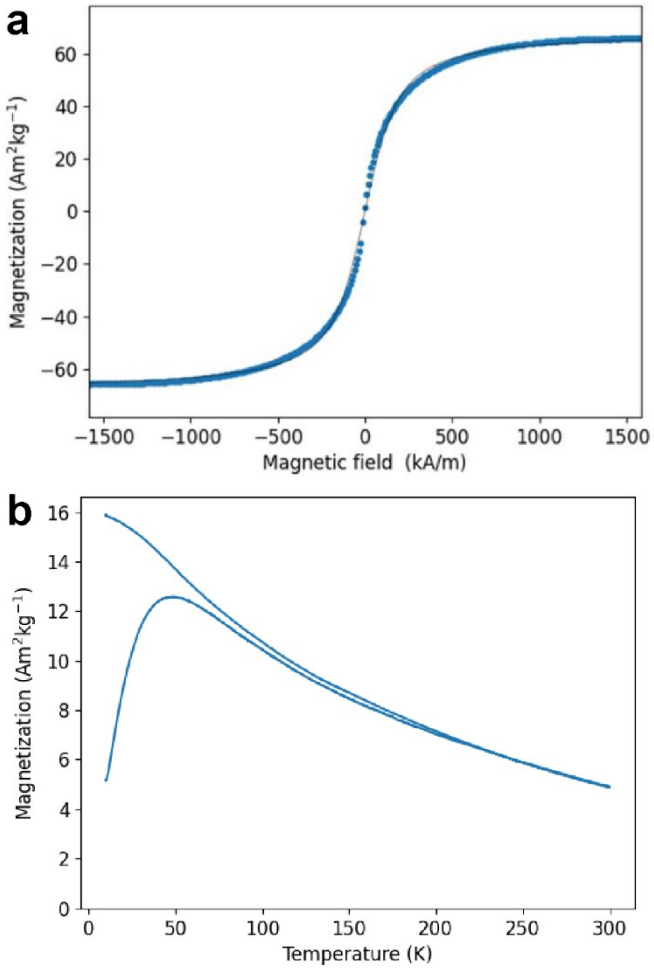

Figure S33. a) Magnetization curve of USPIO(20)@MIL at 300 K (solid black line) and Langevin fit (dotted blue line); b) Magnetic moments of USPIO(20)@MIL (blue line) under an applied magnetic field of 200 Oe after zero field cooling then field cooling.

Table S5. Saturation magnetization and magnetic moments of hybrid nano-objects measured by VSM.

Nanoparticles/nano-objects	M_{sat} 300 K (A $m^2 \cdot kg^{-1}$)	Reference
γ-Fe_2O_3 NPs	49	[1]
USPIO(20) @MIL	68	This work
USPIO(10) @MIL	71	This work
MIL/USPIO(10)	39	[1]
MIL/USPIO-cit(10)	62	[1]
MIL-53(Al)-Fe-AA-13	0.2	[14]
ZIF-8-Fe-AA-CS3	6.3	[14]
ZIF-8-Fe-AA-I3	1.8	[14]
MagNP@PDA@ZIF-8	3.1	[15]

Fe_3O_4@PAA/AuNCs-ZIF-8	8.2	[16]
Fe_3O_4-Au_{25}-ZIF-8	9.1	[6]
Fe_3O_4-ZIF-8	18.9	[7]
Fe_3O_4@PDA@ZIF-90	9.2	[17]
Fe_3O_4@C@MIL-100(Fe)	44.39	[11]
Fe_3O_4@UiO-66	51.58	[18]
Fe_3O_4-COOH@MIL-101(Cr)	10.1	[19]
m-ZIF-90	7	[20]
Fe_3O_4/SiO_2@UiO-66(Zr)	21.7	[21]
Fe_3O_4@SiO_2–MIL-101(Cr)	21	[22]
Fe_3O_4@ZIF-8	14.38	[23]
PEG-NH_2@Fe_3O_4-ZIF-8	6.6	[8]
Fe_3O_4@MOF-808	40.35	[24]
Au-Fe_3O_4@MIL-100(Fe)	53.41	[25]
Fe_3O_4@ZIF-8	54.6	[26]
USPIO/MIL-101(Fe)-NH_2	30	[12]

17-Statistical Analysis

The results are represented as means ± SD. A minimum sample number of 3 was employed to ensure statistical power. Statistical analysis was performed by using two-tailed Student's t test for two groups. P values > 0.05 represented nonsignificance (N.S.). P values < 0.05 represented statistically significant, P values: *p < 0.05, **p < 0.01, ***p < 0.001 (unpaired, two-tailed t tests).

18-References

1 S. Sene, M. T. Marcos-Almaraz, N. Menguy, J. Scola, J. Volatron, R. Rouland, J.-M. Grenèche, S. Miraux, C. Menet, N. Guillou, F. Gazeau, C. Serre, P. Horcajada, N. Steunou, Maghemite-nanoMIL-100(Fe) Bimodal Nanovector as a Platform for Image-Guided Therapy, *Chem,* 2017, **3**, 303-322.

2 Q. L. Vuong, J. F. Berret, J. Fresnais, Y. Gossuin, O. Sandre, A Universal Scaling Law to Predict the Efficiency of Magnetic Nanoparticles As MRI T_2-Contrast Agents, *Adv. Healthcare Mater.,* 2012**,** **1**, 502-512.

3 A. J. Trotier, W. Lefrancois, K. Van Renterghem, J. M. Franconi, E. Thiaudiere, S. Miraux, Positive Contrast High-Resolution 3D-Cine Imaging of the Cardiovascular System in Small Animals Using a UTE Sequence and Iron Nanoparticles at 4.7, 7 and 9.4 T, *J. Cardiovasc. Magn. Reson.,* 2015, **17**, 1-10.

4 M. F. Casula, P. Floris, C. Innocenti, A. Lascialfari, M. Marinone, M. Corti, R. A. Sperling, W. J. Parak, C. Sangregorio, Magnetic Resonance Imaging Contrast Agents Based on Iron Oxide Superparamagnetic Ferrofluids, *Chem. Mater.,* 2010**,** **22**, 1739-1748.

5 A. Kostopoulou, S. K. Velu, K. Thangavel, F. Orsini, K. Brintakis, S. Psycharakis, A. Ranella, L. Bordonali, A. Lappas, A. Lascialfari, Colloidal Assemblies of Oriented Maghemite Nanocrystals and Their NMR Relaxometric Properties, *Dalton Trans.,* 2014, **43**, 8395-8404.

6 D. Yang, G. Yang, S. Gai, F. He, G. An, Y. Dai, R. Lv, P. Yang, Au_{25} Cluster Functionalized Metal-Organic Nanostructures for Magnetically Targeted Photodynamic/Photothermal Therapy Triggered by Single Wavelength 808 nm Near-Infrared Light, *Nanoscale,* 2015, **7**, 19568-19578.

7 J. Lin, P. Xin, L. An, Y. Xu, C. Tao, Q. Tian, Z. Zhou, B. Hu, S. Yang, Fe_3O_4-ZIF-8 Assemblies As pH and Glutathione Responsive T_2-T_1 Switching Magnetic Resonance Imaging Contrast Agent for Sensitive Tumor Imaging *In Vivo*, *Chem. Commun.,* 2019**,** **55**, 478-481.

8 R. Ettlinger, N. Moreno, N. Ziółkowska, A. Ullrich, H. -A. Krug von Nidda, D. Jirák, K. Kerl, H. Bunzen, *In Vitro* Studies of Fe_3O_4 -ZIF-8 Core-Shell Nanoparticles Designed as Potential Theragnostics, *Part. Part. Syst. Charact.,* 2020, **37**, 2000185.

9 Y. Meng, D. Zhang, X. Chen, Z. Dai, X. Yao, P. Cui, D. Yu, G. Zhang, X. Zheng, FePt Nanoparticles Embedded in Metal–Organic Framework Nanoparticles for Tumor Imaging and Eradication, *ACS Appl. Nano Mater.,* 2020, **3**, 4494-4503.

10 S. Dehghani, N. R. Alam, S. Shahriarian, T. Mortezazadeh, S. Haghgoo, A. Golmohamadpour, B. Majidi, M. Khoobi, The Effect of Size and Aspect Ratio of Fe-MIL-88B-NH_2 Metal-Organic Frameworks on Their Relaxivity and Contrast Enhancement Properties in MRI: *In Vitro* and *In Vivo* Studies, *J. Nanopart. Res,* 2018, **20**, 1-16.

11 D. Wang, J. Zhou, R. Chen, R. Shi, G. Xia, S. Zhou, Z. Liu, N. Zhang, H. Wang, Z. Guo, Q. Chen, Magnetically Guided Delivery of DHA and Fe Ions for Enhanced Cancer Therapy Based on pH-Responsive Degradation of DHA-Loaded Fe_3O_4@C@MIL-100(Fe) Nanoparticles, *Biomaterials,* 2016, **107**, 88-101.

12 Z. Xu, Y. Chen, M. Chen, W. Chen, Y. Cheng, Y. Assembly of USPIO/MOF Nanoparticles with High Proton Relaxation Rates for Ultrasensitive Magnetic Resonance Sensing, *J. Mater. Chem. C,* 2021, **9**, 11915-11923.

13 P. Prene, E. Tronc, J. Jolivet, J. Livage, R. Cherkaoui, M. Nogues, J. Dormann, D. Fiorani, Magnetic Properties of Isolated γ-Fe_2O_3 Particles, *IEEE Trans. Magn.,* 1993, **29**, 2658-2660.

14 Y. N. Wu, M. Zhou, S. Li, Z. Li, J. Li, B. Wu, G. Li, F. Li, X. Guan, Magnetic Metal-Organic Frameworks: γ-Fe_2O_3@MOFs *Via* Confined *In Situ* Pyrolysis Method for Drug Delivery. *Small,* 2014, **10**, 2927-2936.

15 J. Zhou, P. Wang, C. Wang, Y. T. Goh, Z. Fang, P. B. Messersmith, H. Duan, Versatile Core-Shell Nanoparticle@Metal-Organic Framework Nanohybrids: Exploiting Mussel-Inspired Polydopamine for Tailored Structural Integration, *ACS Nano,* 2015, **9**, 6951-6960.
16 R. Bian, T. Wang, L. Zhang, L. Li, A Combination of Tri-Modal Cancer Imaging and *In Vivo* Drug Delivery by Metal-Organic Framework Based Composite Nanoparticles. *Biomater. Sci.,* 2015, **3**, 1270-1278.
17 J. Chen, J. Liu, Y. Hu, Z. Tian, Y. Zhu, Metal-Organic Framework-Coated Magnetite Nanoparticles for Synergistic Magnetic Hyperthermia and Chemotherapy with pH-Triggered Drug Release, *Sci. Technol. Adv. Mater.,* 2019, **20**, 1043-1054.
18 H. X. Zhao, Q. Zou, S. K. Sun, C. Yu, X. Zhang, R. J. Li, Y. Y. Fu, Theranostic Metal-Organic Framework Core-Shell Composites for Magnetic Resonance Imaging and Drug Delivery, *Chem. Sci.,* 2016, **7**, 5294-5301.
19 J. P. Wei, B. Qiao, W. J. Song, T. Chen, F. li, B. Z. Li, J. Wang, Y. Han, Y. F. Huang, Z. J. Zhou, Synthesis of Magnetic Framework Composites for the Discrimination of Escherichia Coli at the Strain Level, *Anal. Chim. Acta,* 2015, **868**, 36-44.
20 J. Fang, Y. Yang, W. Xiao, B. Zheng, Y. B. Lv, X. L. Liu, J. Ding, Extremely Low Frequency Alternating Magnetic Field-Triggered and MRI-Traced Drug Delivery by Optimized Magnetic Zeolitic Imidazolate Framework-90 Nanoparticles, *Nanoscale,* 2016, **8**, 3259-3263.
21 W. Zhang, Z. Yan, J. Gao, P. Tong, W. Liu, L. Zhang, Metal-Organic Framework Uio-66 Modified Magnetite@Silica Core-Shell Magnetic Microspheres for Magnetic Solid-Phase Extraction of Domoic Acid from Shellfish Samples, *J. Chromatogr. A,* 2015**, 1400**, 10-18.
22 S. H. Huo, X. P. Yan, Facile Magnetization of Metal-Organic Framework MIL-101 for Magnetic Solid-Phase Extraction of Polycyclic Aromatic Hydrocarbons in Environmental Water Samples, *Analyst,* 2012, **137**, 3445-3451.
23 J. Zheng, C. Cheng, W.-J. Fang, C. Chen, R.-W. Yan, H.-X. Huai, C.-C. Wang, Surfactant-Free Synthesis of a Fe_3O_4@ZIF-8 Core–Shell Heterostructure for Adsorption of Methylene Blue, *CrystEngComm,* 2014, **16**, 3960-3964.
24 Y. Jia, Y. Wang, M. Yan, Q. Wang, H. Xu, X. Wang, H. Zhou, Y. Hao, M. Wang, Fabrication of Iron Oxide@MOF-808 as a Sorbent for Magnetic Solid Phase Extraction of Benzoylurea Insecticides in Tea Beverages and Juice Samples, *J. Chromatogr. A,* 2020, **1615**, 460766.
25 F. Ke, L. Wang, J. Zhu, Multifunctional Au-Fe_3O_4@MOF Core-Shell Nanocomposite Catalysts with Controllable Reactivity and Magnetic Recyclability, *Nanoscale,* 2015, **7**, 1201-1208.
26 T. Zhang, X. Zhang, X. Yan, L. Kong, G. Zhang, H. Liu, J. Qiu, K. L. Yeung, Synthesis of Fe_3O_4@ZIF-8 Magnetic Core–Shell Microspheres and Their Potential Application in a Capillary Microreactor, *Chem. Eng. J.,* 2013, **228**, 398-404.